nanoenergy advances

MDPI

Article

Optoelectronic Properties and Photocatalytic Activity of Cu-Doped Zinc Chalcogenides: A First-Principles Study

Michele Loriso and Francesco Ambrosio *

Dipartimento di Scienze di Base e Applicate (DiSBA), Università degli Studi della Basilicata, Viale dell'Ateneo Lucano, 10, 85100 Potenza, Italy; michele.loriso@unibas.it
* Correspondence: francesco.ambrosio@unibas.it

Abstract

A comprehensive first-principles investigation of bulk and surface Cu defects in Zn-based chalcogenides (ZnO, ZnS, and ZnSe) is presented, aimed at assessing the effect of Cu doping on the optoelectronic properties of these materials and at addressing the photocatalytic activity towards the hydrogen evolution reaction (HER). Defect formation energies, adiabatic and optical charge-transition levels of the bulk materials are determined, and their dependence on growth conditions and Fermi-level position is analysed. The results indicate that, whereas ZnO supports both donor- and acceptor-like Cu defects with pronounced Jahn-Teller distortions, ZnS and ZnSe predominantly stabilise substitutional Cu as a mid-gap acceptor with weaker electron-lattice coupling and similar absolute transition levels. Calculated vertical transition energies rationalise the characteristic emission of Cu-doped samples in terms of defect-mediated optical cycles. The focus is then placed on surface energetics, which differ markedly from bulk behaviour and critically influence photocatalytic performance. Explicit modelling of HER demonstrates that Cu substitution dramatically reduces the overpotential on ZnS and ZnSe by tuning hydrogen adsorption toward the Sabatier optimum, while in ZnO the beneficial effect of Cu doping is diminished by the excessive strengthening of the adsorbate-surface interactions. Finally, the measured HER activities are rationalised by proposing a defect-mediated mechanism involving electron trapping at the surface Cu site, cooperative proton adsorption, and hydride formation. These findings establish defect thermodynamics and surface charge localisation as key design parameters for optimising materials engineering strategies in photocatalytic applications.

Keywords: defect chemistry; density functional theory; heterogeneous photocatalysis; hydrogen evolution reaction

Check for updates

Received: 13 February 2026
Revised: 7 April 2026
Accepted: 29 April 2026
Published: 22 May 2026

Copyright: © 2026 by the authors. Licensee MDPI, Basel, Switzerland. This article is an open access article distributed under the terms and conditions of the Creative Commons Attribution (CC BY) license.

1. Introduction

Zinc chalcogenides of general formula ZnX (X = O, S, Se, Te) are wide band-gap semiconductors of great potential for a variety of applications [1–4]. These include but are not limited to light-emitting diodes, photovoltaics, transparent thin film transistors, and photocatalytic devices [5–10]. In particular, recent applications of ZnO, ZnS, and ZnSe in heterogeneous photocatalysis have been prompted by their suitable band alignment against redox potentials associated with reactions of interest, such as water splitting, nitrogen fixation and a reduction in carbon dioxide [11–14]. Furthermore, their high water resistance and stability [15,16], coupled with ease of deposition on different substrates [17,18], make these materials ideal as overlayers, used to protect the light-absorbing elements of the photocatalytic system [19–21].

In this framework, materials engineering strategies are usually implemented in the attempt to boost the performance of ZnX-containing systems [6,22]. In particular, heteroatom doping can be effectively deployed in order to (i) achieve the desired type of conductivity [23,24], (ii) reduce the band gap of these materials, thus extending their absorption capacity in the visible region of the spectrum [25,26], and (iii) enhance the photocatalytic efficiency by providing catalytic sites for reactions at the semiconductor-water interface [27,28]. Among the plethora of possibilities, the doping of zinc chalcogenides with Cu has received considerable attention [29–32]: with copper being directly on the left side of zinc in the Periodic Table, it is expected to be easily incorporated, due to the minimal lattice mismatch, and to provide shallow defect energy levels and adapt to improve the opto-electronic properties of these semiconductors [33]. Specifically, seminal studies on Cu doping in zinc chalcogenides aimed to achieve *p*-type conductivity, which was found to be quite challenging, since these materials tend to be native *n*-type semiconductors [34,35]. For instance, while ZnS and ZnSe have been *p*-doped via Cu insertion [36,37], this method was found to be unsuccessful for ZnO [38–40], thus hinting at sensitive differences in the defect physics of Cu in ZnX materials [31]. Cu-doped ZnX samples have also sparkled interest in the research community for their peculiar photoluminescence (PL), if compared to those of the pristine materials: ZnO and ZnS were found to show distinct green emission [29,41], whereas a Cu-related red band was observed for ZnSe [42]. Different interpretations of the measured signals have been proposed, but a consensus has not been reached yet: for ZnO, the originally proposed mechanism involving a Cu acceptor state (see Ref. [29]) has recently been questioned, on the basis of *ab initio* calculations, suggesting the involvement of donor states [39,43]. At variance with this, ZnS and (particularly) ZnSe have been far less studied and, while the experimental emission is thought to be related to Cu levels [44], a precise mechanism has not been defined yet; also, because of the wide variability in the reported PL spectra, e.g., Cu-doped ZnS samples may also feature red luminescence [45]. Finally, it is well documented that Cu incorporation in the lattice of zinc chalcogenides has a marked impact on their photocatalytic properties. The inclusion of Cu in ZnO was found to be highly concentration-dependent, with a low–moderate (abundant) addition of copper improving (deteriorating) the photoconversion efficiency [46–50]. Similar considerations have also been advanced for ZnS and ZnSe, with a particular focus on the careful control required to tune the optimal percentage of Cu and avoid the formation of secondary phases [51–53]. In this context, it is worth noting that Cu doping of ZnO was observed to produce a roughly six-fold increase in photocatalytic H_2 production, from ≈7.5 to ≈41.5 μmol $g^{-1}h^{-1}$ [49], while higher rates may be achieved using sacrificial agents, e.g., glycerol in Ref. [46]. The effect was found to be substantially more pronounced for ZnS: Cu-enriched samples have recently been found to reach H_2 conversion rates of up to 8 mmol $g^{-1}h^{-1}$, compared with the tenths of μmol $g^{-1}h^{-1}$ produced by the pristine material, signalling an improvement of up to three orders of magnitude [54–57]. Such a large difference calls for an in-depth analysis of the defect physics and the reaction mechanism at the heterogeneous interface.

In this work, a comprehensive and comparative first-principles investigation of Cu defects in ZnO, ZnS, and ZnSe is presented, addressing their bulk and surface energetics, electronic structure, optical signatures, and their role in the hydrogen evolution reaction (HER). By combining a rigorous grand-canonical treatment of charged defects with hybrid density functional theory (DFT) and the computational hydrogen electrode approach, the study reveals a qualitative distinction between ZnO and the heavier chalcogenides. Whereas ZnO supports both donor- and acceptor-like Cu defects with pronounced electron–lattice coupling and Jahn–Teller distortions, ZnS and ZnSe exhibit a markedly different defect physics, characterised by substitutional Cu acting as a mid-gap acceptor with similar absolute charge-transition levels in the two hosts and interstitial Cu being largely electrically inactive in the bulk. The reduced ionicity and enhanced covalency of ZnS and ZnSe drives a transition from hole localisation in ZnO to electron trapping. At surfaces, defect energetics and charge-transition levels are substantially modified with respect to the bulk, with important implications for photocatalytic activity.

Building on this defect-level analysis, the HER mechanism on pristine and Cu-doped surfaces is explicitly modelled. It is shown that the catalytic response is governed by how Cu incorporation reshapes hydrogen adsorption thermodynamics: in ZnO, doping reinforces already strong H binding and increases the overpotential, whereas in ZnS and ZnSe, it stabilises otherwise weak adsorption and drives the system toward the Sabatier optimum. On this basis, a defect-mediated reaction pathway is proposed in which photogenerated electrons are trapped at surface substitutional Cu, enabling cooperative proton adsorption and subsequent hydride formation at the surface. Modelling of the reaction steps within such a mechanism explains the superior performance for HER of Cu-doped ZnS with respect to ZnO and further advances ZnSe as a viable alternative to be used in photocatalytic devices well. Overall, this work connects defect thermodynamics, optical activity, and catalytic performance, providing a coherent picture of Cu doping in Zn chalcogenides and establishing defect engineering as a strategy to tune hydrogen adsorption and photocatalytic functionality in wide band-gap semiconductors.

The remainder of this paper is organised as follows: In Section 2, a theoretical framework, which takes advantage of electronic-structure calculations, is described to calculate (i) the formation energy and relevant energy levels of Cu defects in the bulk of zinc chalcogenides and at their surface, and (ii) the overpotential associated with the HER taking place at the surface of ZnX materials. Section 3 provides the computational details for the large variety of electronic-structure calculations carried out in this work; Section 4 presents and critically discusses the key results of the investigation. Finally, Section 5 summarises the main conclusions of this work.

2. Theory

2.1. Formation Energies of Cu Defects in ZnX Chalcogenides

In order to describe the energetics and electronic properties of Cu defects in ZnX materials from first principles, the grand-canonical formulation of defects in crystalline materials is employed [58,59], which allows for a proper evaluation of their formation energies. Within this theoretical context, the formation energy of a defect, X, with charge state q in the relaxed nuclear coordinates R_q, $E_f[X^q(R_q)]$, is provided by the following equation [58–60]:

$$E_{\mathrm{f}}[X^q(R_q)] = E[X^q(R_q)] - E[\mathrm{bulk}] + \textstyle\sum_i n_i\mu_i + q(\epsilon_V + \mu_e) + E_{\mathrm{corr}}(R_q, q), \tag{1}$$

where $E_{\mathrm{f}}[X^q(R_q)]$ is the total energy of a periodic supercell containing the defect X^q, $E[\mathrm{bulk}]$ the total energy of the pristine bulk supercell. The summation term $\sum_i n_i\mu_i$ holds the chemical potentials of the species i, μ_i, which are added (subtracted) to (from) the bulk material n_i times. Given that the formation energies of Cu defects are constrained by the chemical potentials of the components of ZnX chalcogenides, as well as by that of the dopant itself (i.e., μ_{Zn}, μ_{X}, and μ_{Cu}), their evaluation is of great importance to establish the defect formation energies under different growth conditions [cf. Section S1 of the Supplementary Information (SI) for details]. The term $\epsilon_V + \mu_e$, entailing the valence band maximum (VBM) of the perfect material and the chemical potential of the electron, is required by the grand-canonical ensemble when dealing with charged defects and defines the electron reservoir. $E_{\mathrm{corr}}(R_q, q)$ is an energy correction to be applied to the DFT total energy of a charged supercell containing localised electron density, whose purpose is to obviate the spurious electrostatic interaction among periodic replicas [58,59,61]. According to the Freysoldt–Neugebauer–Van de Walle correction scheme [58,59], employed in this work, this term corresponds to the model correction for a charge q screened by the static dielectric constant ϵ_0:

$$E_{\mathrm{corr}}(R_q, q) = E_m(q, \epsilon_0). \tag{2}$$

Correction terms up to 0.16 (0.11) eV are calculated for the charged supercells of ZnS (ZnSe) used in this study, adopting the experimental values of ϵ_0 (8.32 for ZnS and 9.2 for ZnSe [62]). An evaluation of the different terms in Equation (1) for each studied charge state allows us to assess:

- The adiabatic charge transition levels (CTLs), defined as the electron chemical potential that satisfies $E_{\mathrm{f}}[X^q(R_q)] = E_{\mathrm{f}}[X^{q'}(R_{q'})]$ [58,59]:

  $$\mu^{\mathrm{ad}}_{q/q'} = \frac{E_{\mathrm{f}}[X^q(R_q)] - E_{\mathrm{f}}[X^{q'}(R_{q'})]}{q'-q} + \frac{E_{\mathrm{corr}}(R_q, q) - E_{\mathrm{corr}}(R_{q'}, q')}{q'-q} - \epsilon_{\mathrm{V}}. \tag{3}$$

  Equation (3) allows the definition of eventual donor or acceptor defect levels in the band gaps of the studied semiconductors, which in turn can be related with the measured electronic properties.
- Vertical charge transition levels involving the defect in the charge states q and q' at fixed R_q or R'_q coordinates, which can be connected with spectroscopic signatures of defects in semiconductors [39,43,44], are defined as:

  $$\mu^{\mathrm{opt}}_{q \to q'} = \frac{E_{\mathrm{f}}[X^q(R_q)] - E_{\mathrm{f}}[X^{q'}(R_q)]}{q'-q} + \frac{E_{\mathrm{corr}}(R_q, q) - E_{\mathrm{corr}}(R_q, q')}{q'-q} - \epsilon_{\mathrm{V}}, \tag{4}$$

  where $E_{\mathrm{corr}}(R_q, q')$ is the electrostatic finite-size correction of the supercell associated with the defect in the relaxed coordinates R_q vertically brought to the charge state q' (i.e., upon oxidation/reduction). The latter term is calculated according to the method developed in Ref. [61], which provides the following operative definition:

  $$E_{\mathrm{corr}}(R_q, q') = E_{\mathrm{m}}(q, \epsilon_0) - E_m(q + q_{\mathrm{pol}}, \epsilon_\infty) + E_{\mathrm{m}}(q' + q_{\mathrm{pol}}, \epsilon_\infty), \tag{5}$$

  where ϵ_∞ is the high-frequency dielectric constant of the material and q_{pol} the ionic polarisation charge, defined as:

  $$q_{\mathrm{pol}} = -q\left(1 - \frac{\epsilon_0}{\epsilon_\infty}\right). \tag{6}$$

The calculated correction terms for the supercells employed in this study are found to exiguous (below 0.1 eV in all the studied cases).

Adiabatic energy levels for the ZnS and ZnSe surfaces are determined according to the Equation (3), with the sole differences being that ϵ_{V} now refers to the valence band edge of the pristine slab and that a different technique is employed to correct the electrostatic finite-size error. In this case, a method which accounts for the varying dielectric profile across the semiconductor-vacuum interface is employed, defining the correction as [63]:

$$E^{\mathrm{slab}}_{\mathrm{corr}}(R_q, q) = E_{\mathrm{iso}} - E_{\mathrm{per}} + q\Delta V, \tag{7}$$

where E_{per} and E_{iso} are the electrostatic energies of the slab and that of the isolated charge (under the assumption of uniform scaling of all dimensions of the supercell, including the vacuum layer), and ΔV is an alignment term which accounts for the shift between DFT potentials and model. Higher corrections up to 0.4 eV are calculated for charged slabs with this method, as a consequence of the reduced screening.

2.2. Hydrogen Evolution Reaction at the Surfaces of Zinc Chalcogenides

HER on the surfaces of zinc chalcogenides is investigated according to the DFT-based computational hydrogen electrode (CHE) approach outlined in Refs. [64,65], which has been extensively employed in the description of electrochemical processes via the modelling of reaction intermediates [66–69]. The CHE is based on the assumption that the reduction reaction affording gaseous hydrogen:

$$H^+(aq) + e^- \rightleftharpoons \tfrac{1}{2}H_2(g) \tag{8}$$

is reversible (i.e., $\Delta G_0 = 0$) at the potential of the standard hydrogen electrode (SHE) at 298 K, $1.0 \cdot 10^5$ Pa and pH $= 0$. In these conditions, the following equality holds:

$$\mu[H^+(aq)] + \mu[e^-] = \tfrac{1}{2}\mu[H_2(g)], \tag{9}$$

which effectively allows for the replacement of the chemical potentials of $H^+(aq)$ and e^- with that of $H_2(g)$. The HER is then modelled via a two-step process outlined as follows:

$$\begin{gathered} * + H^+(aq) + e^- \rightleftharpoons H^*_{ads} \\ H^*_{ads} + H^+(aq) + e^- \rightleftharpoons * + H_2(g), \end{gathered} \tag{10}$$

where the chemical specimen denoted as an asterisk (*) refers to an active site on the surface of ZnX. The Gibbs free energy variation for the first step, ΔG_1, can be written as:

$$\Delta G_1 = \mu[H^*_{ads}] - \mu[*] - \mu[H^+(aq)] - \mu[e^-], \tag{11}$$

and consequently, from Equation (9):

$$\Delta G_1 = \mu[H^*_{ads}] - \mu[*] - \tfrac{1}{2}\mu[H_2(g)], \tag{12}$$

whereas:

$$\Delta G_2 = \Delta G_0 - \Delta G_1 = -\Delta G_1. \tag{13}$$

The value of ΔG_1 and, in turn, that of ΔG_2 are influenced by the adsorption energies of H species on the surface of the catalyst: strong (weak) adsorption leads to more negative (positive) values for ΔG_1 (ΔG_2). The overpotential of the HER process, η_{HER}, can then be defined as [69]:

$$\eta_{HER} = \frac{|\Delta G_1|}{e} \tag{14}$$

The value of each chemical potential in Equation (11) can be approximately defined as [70]:

$$\mu = E^{DFT} + ZPE - TS + \Delta U^{0\to T}. \tag{15}$$

In Equation (15), E^{DFT} is the DFT total energy of the system, ZPE is the zero-point energy of the free or adsorbed species, calculated under the harmonic approximation. S is the entropy of the system which, for the free species, entails rotational, vibrational, and translational contributions. For adsorbed species, the entropy S includes solely the vibrational term. $\Delta U^{0\to T}$ is the variation of internal energy accompanying the temperature change from 0 K (i.e., the reference temperature of DFT total energies) to T. Overall, the latter contributions allows conversion of DFT total energies into Gibbs free energies at finite temperature. It is

https://doi.org/10.3390/nanoenergyadv6020017

noted that uncertainty in hydrogen adsorption free energies within the CHE computational framework is typically on the order of 0.1 eV, based on comparisons between DFT and experiment [71]. Furthermore, solvent-related effects are generally below 0.2 eV for H adsorption [72]. The precise definition of each term in Equation (15) and the respective calculated values for the systems under investigation in this study are given in Section S2 of the SI.

3. Computational Details

Section S3 of the SI reports the structural parameters of the supercells and slab models employed to investigate the defect physics and the HER mechanism on ZnX chalcogenides, as well as those of metallic Zn, Cu, and competing phases, which are essential for the definition of the chemical potentials in Equation (1). In all cases, geometry optimisation are carried out, by relaxing the position of the nuclei while preserving the lattice constants of each material to the experimental value. In particular, bulk ZnS and ZnSe are modelled employing $3 \times 3 \times 3$ supercells containing 216 atoms. Doped systems are investigated (i) substituting a single lattice Zn with Cu, in the case of Cu_{Zn}, (ii) adding a single Cu ion in an octahedral void of the supercell for Cu_i. These correspond to Cu concentrations of $2.34 \cdot 10^{20}$ atoms/cm^3 (0.93 at.%) for ZnS and $2.03 \cdot 10^{20}$ atoms/cm^3 (0.93 at.%) for ZnSe, in line with previous work on ZnO [43]. For the slabs, the most stable apolar surfaces are considered, namely the $(10\bar{1}0)$ for ZnO and the (110) for ZnS and ZnSe [73–76]. The Cu concentrations used for slab calculations are $6.04 \cdot 10^{13}$ atoms/cm^2 (1.04 at.%) for ZnS and $5.50 \cdot 10^{13}$ atoms/cm^2 (1.04 at.%) for ZnSe. The investigated Cu defect concentrations are consistent with the experimental values reported in the literature for Cu-doped chalcogenides, for which doping regime is maintained for concentrations below 3–6 at.% [46,48,54], while secondary phases are found to appear above this threshold [23,77,78]. Slab calculations also allow for the alignment of the band edges of the considered semiconductors against the vacuum level via an evaluation of the potential energy profile across the material-vacuum interface (as reported in Section S3 of the SI). This, in turn, permits the definition of absolute charge transition levels from Equations (3) and (4), by referring ϵ_V to the vacuum level.

All DFT calculations are performed with the freely available CP2K-QUICKSTEP package [79–81]. Norm-conserving pseudopotentials developed by Goedecker, Teter and Hutter [82] are employed for modelling core electrons, and MOLOPT double-ζ polarised basis sets [80] are used for valence electrons. Both pseudopotentials and basis sets are specifically designed for hybrid functionals [81]. A cutoff of 600 Ry is set for the plane waves. Hybrid DFT computational costs are alleviated by taking advantage of the auxiliary matrix method [83–85], implemented in CP2K, and by making use of the compact cFIT auxiliary basis set [85], generally yielding results fairly in agreement with those achieved with larger and more computationally expansive sets [86]. The unrestricted Kohn–Sham (UKS) formalism is adopted for all calculations involving unpaired electrons. A piecewise-linear (PWL) hybrid functional of the PBE0 family [87–90] is employed, representing a suitable choice for mitigating the self-interaction error typical of standard DFT methods [91,92], which would otherwise lead to an incorrect description of charge localisation in semiconductors [93]. In particular, for each chalcogenide, the fraction of Fock exchange α satisfying the generalised Koopman condition [94–96] is used, as described in Ref. [97]. Energy levels obtained via the PWL functional are then referenced to the VBM and the CBM of each material, as obtained when tuning the fraction of Fock exchange to reproduce the experimental band gaps. This is done to completely silence the remaining band gap error of the PWL functional (up to 0.8 eV for ZnSe, see Section S3 of the SI), which may affect the evaluation of optical transitions involving both defect energy levels and the band edges of the host materials, in line with previous work [43]. Since it has been proven that charge-transition levels are robust with respect to the fraction of Fock exchange included in global hybrid functionals, this procedure can be safely employed, provided that the band gap is not severely underestimated [86,98–100].

Vibrational frequencies, required to estimate ZPE and vibrational entropy in Equation (15), are computed within the harmonic approximation using the finite displacement method. In order to reduce the computational cost, all substrate atoms are kept fixed, and only the adsorbed H atom is displaced. Consequently, three vibrational modes are obtained for each adsorbed configuration. Energy barriers associated with proton migration from one surface site to another, which are predicted to occur during HER (*vide infra*), are calculated using the linear transit method to construct intermediate structures connecting reactants and products along a linear path [101].

4. Results and Discussion

The properties of Cu defects in the bulk materials are first discussed. It is known that Cu inclusion in ZnX materials may mainly result in either the substitution of lattice Zn (Cu_{Zn} in defects nomenclature) or the interstitial incorporation of the heteroatom inside the octahedral voids of the host (Cu_i) [39,43,102]. For the neutral substitution, Cu^0_{Zn}, entailing d^9 Cu(II), Jahn–Teller distortions cause the four-fold coordinated Cu^{2+} ion to display three roughly equal Cu-X bonds and a longer one [cf. Figure 1a for a schematic representation and Section S4 of the SI for illustration of all the relaxed structures of ZnS and ZnSe]. Upon reduction (oxidation), provided that the electron (hole) is indeed localised on the defect moiety, the distortions are expected to be alleviated, and the bonds are elongated (shrunk), due to the filling (depletion) of anti-bonding orbitals. Similar considerations generally also hold for the interstitial defect [cf. Figure 1b], featuring a highly distorted d^9 Cu_i^{2+} and a less asymmetric microstructure in the reduced/oxidised states. The present results indicate that the extent of Jahn-Teller distortions is found to be strongly material-dependent; see Figure 1c,d. In particular, for Cu^0_{Zn}, a decreasing trend is observed along the chalcogens group, with ZnO featuring the largest difference in bond lengths (≈5%), while the effect is sensitively reduced for ZnS and ZnSe (below 2%). This can be rationalised with the increased covalency of the Cu-S/Se bonds, which reduces the electron-lattice coupling, thereby decreasing the energetic gain from symmetry breaking and leading to progressively weaker distortions from ZnO to ZnSe.

The structural reorganisation upon variation of charge state follows an analogous trend: the reduced Cu^-_{Zn} featuring d^{10} Cu(I), shows a pronounced bond elongation (up to 0.3 Å) in ZnO, while it is exiguous (0.02–0.03 Å) in ZnS and ZnSe. Finally, upon oxidation, no structural change is observed for ZnS and ZnSe [cf. Figure 1c]. Indeed, differently from ZnO, the injected hole does not localise on the defect moiety, as is also confirmed by an inspection of both the spin density, resembling that of Cu^0_{Zn}, and the lowest occupied molecular orbital, showing no localisation (cf. Section S4 of the SI). This is expected to be due to a sizeable difference in the absolute position of band edges among the three materials, with ZnS and ZnSe featuring VBM values much closer to the vacuum level (*vide infra*).

The dissimilarity between ZnO and other chalcogenides is even more marked when the interstitial defect is examined. In fact, in stark contrast with what has been observed for the oxide refs. [39,43], neither Cu_i^{3+} nor Cu_i^{2+} is stable in ZnS and ZnSe. No spin localisation is envisaged for both the charge states (cf. Section S4 of SI), and the structural features of the defect moiety are essentially unchanged with respect to those observed for Cu_i^+ [cf. Figure 1d]. This clearly indicates that the latter, representing d^{10} Cu(I), is the only stable charge state, while d^9 Cu(II) is not supported by these host materials. In fact, for interstitial defects, the absence of a pre-existing Madelung potential minimum leads to a much larger Coulomb penalty for higher charge states, making their stability strongly dependent on the host's ionicity. This justifies the absence of highly charged interstitial defects in the less ionic environment formed by S and Se. Overall, Cu_i can be assumed to be electrically inactive in ZnS and ZnSe.

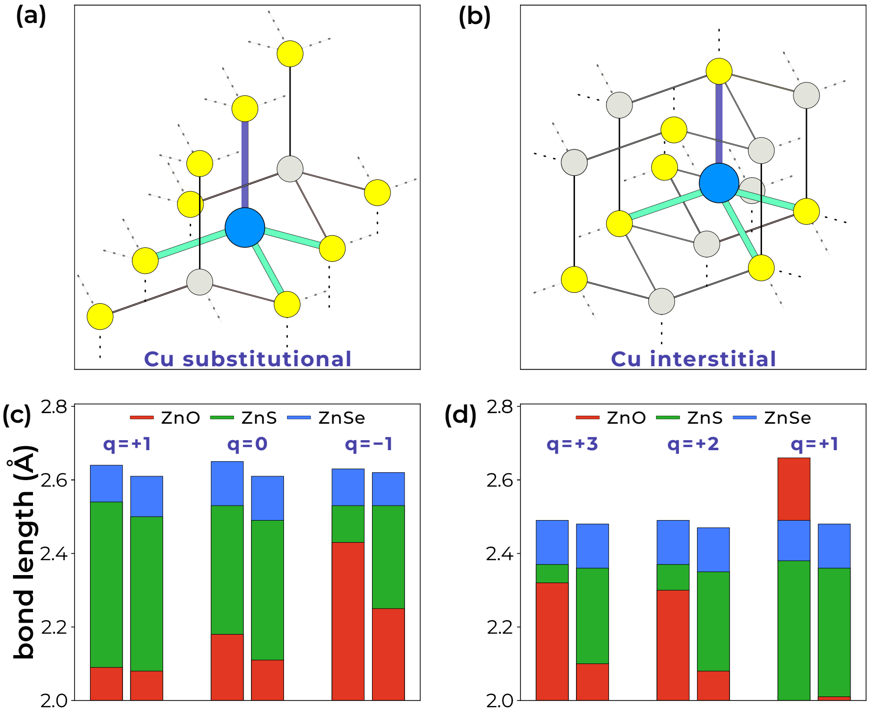

Figure 1. Schematic representation of Cu_{Zn} (**a**) and Cu_i (**b**) in Zn chalcogenides. Cu in blue, Zn in grey, and chalcogen X (O, S, Se) in yellow. Cu-X bonds are highlighted in cyan and blue to distinguish between shorter and longer bonds, respectively, as ensuing from Jahn–Teller distortions, cf. main text. Histogram representation of the longest and shortest Cu-X bond lengths for Cu_{Zn}^{q} [panel (**c**), $q = +1, 0, -1$] and Cu_i^{q} [panel (**d**), $q = +3, +2, +1$]. Data from Ref. [43] are considered for ZnO. Bars are given in red for ZnO, green for ZnS, and blue for ZnSe.

Figure 2a reports the absolute band edges of ZnO, ZnS and ZnSe, along with the charge transition levels of Cu defects. It is first noted that the computational protocol provides highly accurate ionisation potentials and electron affinities of bulk semiconductors, with differences with respect to the experiment below 0.1 eV [103,104], thus ensuring the reliability of the predictions on defect levels. These latter reveal again a contraposition between the oxide and the other chalcogenides: the former presents both deep donor (substitutional) and acceptors (interstitial) levels, while the other materials only feature a mid-gap acceptor level associated with Cu_{Zn} at almost the same absolute position (5.52 vs. 5.57 eV), thus corroborating a physical picture which sees ZnS and ZnSe display a very similar defect physics [31]. Because the $(0/-1)$ transition level lies ≈2 eV (1.4) above the valence band maximum of ZnS (ZnSe), Cu acts as a deep acceptor. Therefore, significant equilibrium *p*-type conductivity from isolated Cu dopants is not expected at room temperature, and the observed *p*-type behaviour is likely associated with non-equilibrium growth conditions, the suppression of compensating donors, or defect complex formation, rather than shallow acceptor ionisation of isolated Cu centers. The evolution of charge transition levels for Cu_{Zn} along the chalcogenides series reflects a crossover in carrier localisation. In ZnO, the strong electron-lattice coupling and the low-lying VBM stabilise hole localisation. In contrast, the increased covalent character of ZnS and ZnSe, along with their higher VBM, suppresses hole trapping while favouring electron localisation. This results in a $(0/-1)$ level within the gap, in line with seminal DFT studies on the subject, in which, nevertheless, the band gap problem of DFT was only partially mitigated [31].

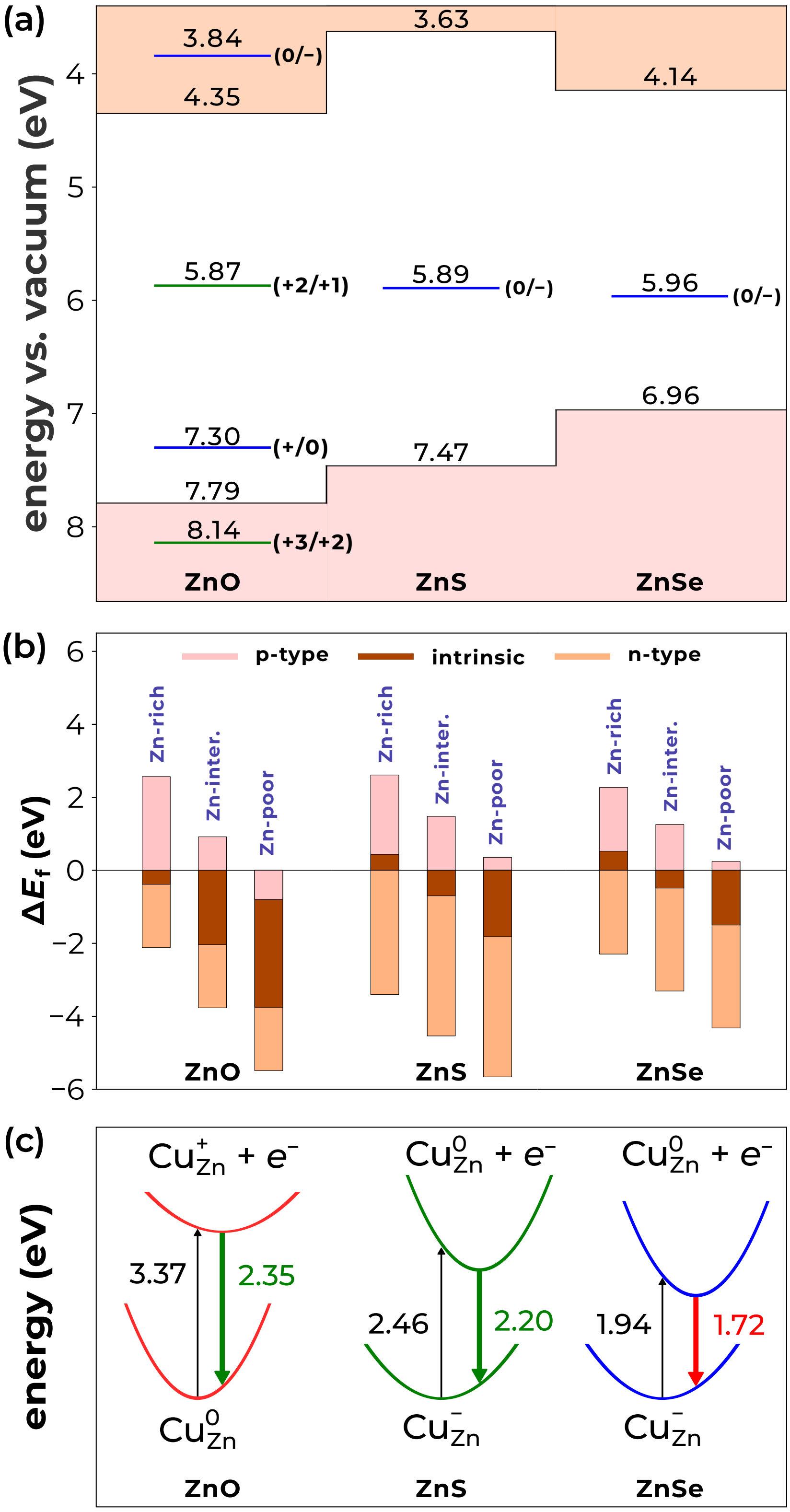

Figure 2. (**a**) Adiabatic charge transition levels of substitutional and interstitial Cu in ZnX materials, represented by blue and green horizontal lines, respectively. Band edges of ZnO, ZnS, and ZnSe, corresponding for each material to the respective experimental value [103,104], are aligned with respect to the vacuum level. (**b**) Calculated values of ΔE_f (cf. main text for definition) for different materials under different growth conditions and considering *p*-type, intrinsic, and *n*-type samples. Negative (positive) values indicate that the substitutional (interstitial) Cu is more stable. (**c**) Configuration coordinate diagrams for $\mathrm{Cu_{Zn}}$ consistent with the experimental characterisation (cf. main text) for different ZnX materials. Data from Ref. [43] are considered for ZnO. All values are given in eV.

Considering the sizeable differences in the electronic properties associated with $\mathrm{Cu_{Zn}}$ and $\mathrm{Cu_i}$ in ZnX, it is of utmost importance to determine how the growth conditions and Fermi levels of the materials can influence the relative abundance of the two defects. To this end, the difference in formation energies between $\mathrm{Cu_{Zn}}$ and $\mathrm{Cu_i}$ is calculated; it depends upon μ_e, the chemical potentials of the constituting elements (Zn and the chalcogen X) and that of the Cu dopant. At fixed atomic and electron chemical potentials, the formation energy difference, considering for each defect the most stable charge states, is defined as:

$$\Delta E_{\mathrm{f}}^{\mathrm{min}}(\mu_e) = E_{\mathrm{f}}^{\mathrm{min}}[\mathrm{Cu}_{\mathrm{Zn}}^{q_s}; \mu_e] - E_{\mathrm{f}}^{\mathrm{min}}[\mathrm{Cu}_{\mathrm{i}}^{q_i}; \mu_e]. \tag{16}$$

In Equation (16), $E_{\mathrm{f}}^{\mathrm{min}}[\mathrm{Cu}_{\mathrm{Zn}}^{q_s}; \mu_e]$ and $E_{\mathrm{f}}^{\mathrm{min}}[\mathrm{Cu}_{\mathrm{i}}^{q_i}; \mu_e]$ are the formation energies calculated for most stable charge state for the substitutional (q_s) and the interstitial (q_i) defect at a given μ_e. These values can be easily extrapolated from formation energy diagrams (see Section S4 for ZnS and ZnSe and Ref. [43] for ZnO). For clarity of presentation, the analysis is restricted to three representative growth conditions (Zn-rich, intermediate, and Zn-poor) and to three limiting regimes of conductivity, namely p-type (Fermi level close to the VBM), intrinsic (mid-gap Fermi level), and n-type (Fermi level close to the CBM). Calculated values, illustrated in the histogram of Figure 2b, shed light on three key aspects:

- Interstitial defects are generally more stable under Zn-rich and stoichiometric conditions, because of the increased cost associated with removing lattice Zn (see Section S1 of SI), thus suggesting that such conditions should be avoided to prevent $\mathrm{Cu_i}$ from being the dominant defect;
- In this framework, it should be noted that $\mathrm{Cu_i}$ is expected to be more abundant in p-type/intrinsic samples, while its concentration should be negligible in the more commonly produced n-type materials;
- Finally, it is evident that $\mathrm{Cu_i}$ is more easily formed in ZnS and ZnSe, with respect to ZnO. This is possibly due to the combined effect of (i) larger octahedral voids attenuating the hindrance associated with ion insertion and (ii) the reduced Coulomb term for ZnS/ZnSe in which the defect is only stable in the +1 charge state.

The present analysis is also connected with the optical properties of Cu-doped ZnX samples. With the interstitial being electrically inactive, it is not expected to contribute directly to the measured PL and instead may be related with the PL drop-off observed at increasing Cu content, refs. [41,42,105] plausibly due to a larger concentration of $\mathrm{Cu_i}$. As a matter of fact, the typical green emission of Cu-doped ZnO and ZnS and the red emission of Cu-enriched ZnSe samples are generally interpreted in terms of optical transitions involving $\mathrm{Cu_{Zn}}$ [39,43,44]. In ZnO, the PL has been demonstrated to originate from radiative recombination between photogenerated $\mathrm{Cu}_{\mathrm{Zn}}^{+}$ and electrons in the CB of ZnO, see Figure 2c [43]. In contrast, the calculations indicate a qualitatively different mechanism in ZnS and ZnSe. Specifically, it is found from the calculated optical levels reported in Section S4 of the SI, that consistency with experimental emission energy is achieved considering a two-step mechanism involving (i) photo-oxidation of $\mathrm{Cu}_{\mathrm{Zn}}^{-}$ and (ii) its subsequent reduction mediated by a photogenerated electron. Within this picture, optical transition levels are estimated at 2.20 eV for ZnS and at 1.72 eV for ZnSe [cf. Figure 2c], both in fair agreement with available measurements and a previous computational study, in which, however, finite-size corrections on optical levels were not accounted for [44]. Naturally, such a mechanism may be operative primarily for n-type materials, where the Fermi level lies closer to the CBM and $\mathrm{Cu}_{\mathrm{Zn}}^{-}$ is the dominant charge state [see Figure 2a]. This physical picture is further supported by seminal electron paramagnetic resonance (EPR) measurements on Cu-doped ZnS and ZnSe, which do not show signals attributable to Cu^{2+} [106,107]. This absence has been interpreted as evidence that substitutional copper should occur predominantly in a compensated Cu^{+} ground state. At the same time, optically detected magnetic resonance (ODMR) experiments demonstrated that Cu^{2+}-like configurations are involved transiently during radiative recombination processes [107], in full agreement with the present computational characterisation. Conversely, it is predicted that an enhanced p character of the material may result in lower-energy emission. Under the assumption that Cu_{Zn}^{0} in ZnS (ZnSe) is present in the electrically neutral sample, the energy of the photons emitted upon vertical oxidation of photo-generated Cu_{Zn}^{-} is estimated to be ≈1.40 (0.9) eV (see Section S4 of SI). Therefore, variations in growth conditions, unintentional doping, or post-growth treatments that shift the Fermi level may thus change the relative weight of competing Cu-related emission channels without altering the chemical identity of the defect. This sensitivity provides a natural framework to rationalise the pronounced variability in the PL spectra reported for Cu-doped ZnX materials, ref. [45] and suggests that control over the electronic environment may be used to selectively favour specific Cu-related optical transitions.

The results achieved for the surface Cu defects, which are potentially relevant to the photocatalytic properties of doped zinc chalcogenides, are next presented. As in the bulk, Cu at ZnX surfaces can occur in both substitutional and interstitial configurations, and in all cases considered here, the defect is undercoordinated. In particular, in Cu_{Zn}^{0}, i.e., charge neutral substitution, Cu presents a somewhat distorted configuration characterised by one longer and two shorter bonds for all investigated chalcogenides; see Figure 3a for a schematic representation of substitutional Cu doping on the $(10\bar{1}0)$ surface of ZnO and on the (110) surface of ZnS and ZnSe. Again, the elongation/shortening of these bonds are expected upon reduction/oxidation, as monitored by the analysis of the bond lengths presented in Figure 3b. While the expected trend holds for the negatively charged Cu_{Zn}^{-}, no appreciable geometry relaxation is observed upon hole injection for ZnS and ZnSe. This indicates that, similarly to the bulk, the surface defect does not trap the positive charge, which is instead delocalised in a VB state (as is also evident from the isodensity representations reported in Section S5 of the SI) The defect chemistry of surface interstitial Cu is more complex and host-dependent: on the apolar $(10\bar{1}0)$ of ZnO, the extra Cu atom is found to display two-fold coordination, as it bridges two undercoordinated O atoms, cf Figure 3a, with the predicted differences in bond lengths across different charge states [see Figure 3c]. Interestingly, on the ZnS and ZnSe (110) surfaces, the interstitial Cu atom adopts a mixed coordination environment, forming two bonds with surface chalcogen atoms and an additional bond with a surface Zn atom [see Figure 3a]. Surface Cu_{i}^{q} is found to be stable in both the $q = +2$ and $q = +1$ charge states, corresponding to d^{9} Cu(II) and d^{10} Cu(I), respectively, again with marked differences in bond lengths, cf. Figure 3c. This behaviour can be attributed to the reduced coordination and enhanced structural flexibility, of the surface defect: in particular, the formation of a mixed Cu-X/Cu-Zn coordination at the surface provides an efficient stabilisation mechanism for Cu_{i}^{2+}, as it allows partial charge delocalisation and enhanced local screening, which in turn lower the energetic cost associated with the higher oxidation state.

The peculiar features of surface defects are reflected in charge transition levels displaying large shifts with respect to their bulk counterparts, cf. Figure 4a. In particular, for ZnO, the $(0/-1)$ acceptor level of the substitutional defect is shifted at higher energies (by ≈0.4–0.5 eV) and, hence, inside the band gap. This transition level is instead pushed towards the vacuum level for ZnS and ZnSe, and such a result is consistent with a larger stability region for the oxidised Cu^{2+} ion, when assimilated at the surface. The surface-induced variations are even more marked for Cu_{i}, which becomes inactive as an acceptor on the ZnO $(10\bar{1}0)$ surface. Conversely, surface Cu_{i} gives rise to (+2/+1) energy levels at 4.32 and 4.22 eV below the vacuum level on the (110) surfaces of ZnS and ZnSe, respectively.

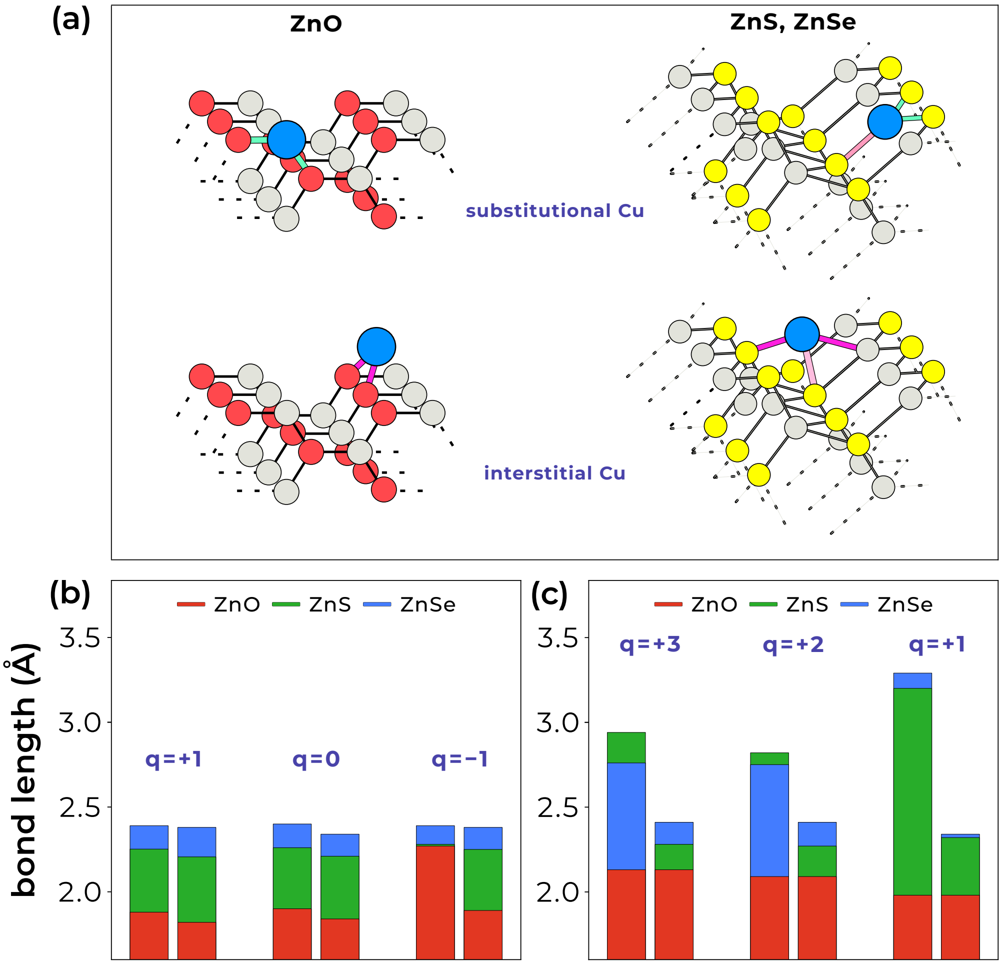

Figure 3. (**a**) Schematic representation of surface Cu$_{\text{Zn}}$ and Cu$_{\text{i}}$ in Zn chalcogenides. Cu in blue, Zn in grey, O in red, and Se/S in yellow. Cu-X and Cu-Zn bonds are highlighted. The left panels display the illustration for the defects on the $(10\bar{1}0)$ surface of ZnO, right panels for the (110) surfaces of ZnS and ZnSe. Histogram representation of the longest and shortest Cu-X bond lengths for surface Cu$^{\text{q}}_{\text{Zn}}$ [panel (**b**), $q = +1, 0, -1$] and surface Cu$^{\text{q}}_{\text{i}}$ [panel (**c**), $q = +3, +2, +1$]. Data from Ref. [43] are considered for ZnO. Bars are given in red for ZnO, green for ZnS, and blue for ZnSe.

A re-evaluation of $\Delta E_{\text{f}}^{\text{min}}(\mu_e)$ [cf. Figure 4b] for the surface defects shows that the stability region of the interstitial is widened for ZnO, whereas it is shrunken for ZnS and ZnSe, with respect to the bulk. In detail, for the heavier chalcogenides, the surface interstitial is expected to be appreciably present only in materials with pronounced p-type character. In the oxide, the increase in the inert Cu interstitials, at the expense of electrically active substitutional, may be detrimental for interface photocatalytic properties (*vide infra*). At variance, both the substitutional and the interstitial may in principle accept electrons at the (110) surface of ZnS and ZnSe and serve as hot-spots for reactions at the heterogeneous interface.

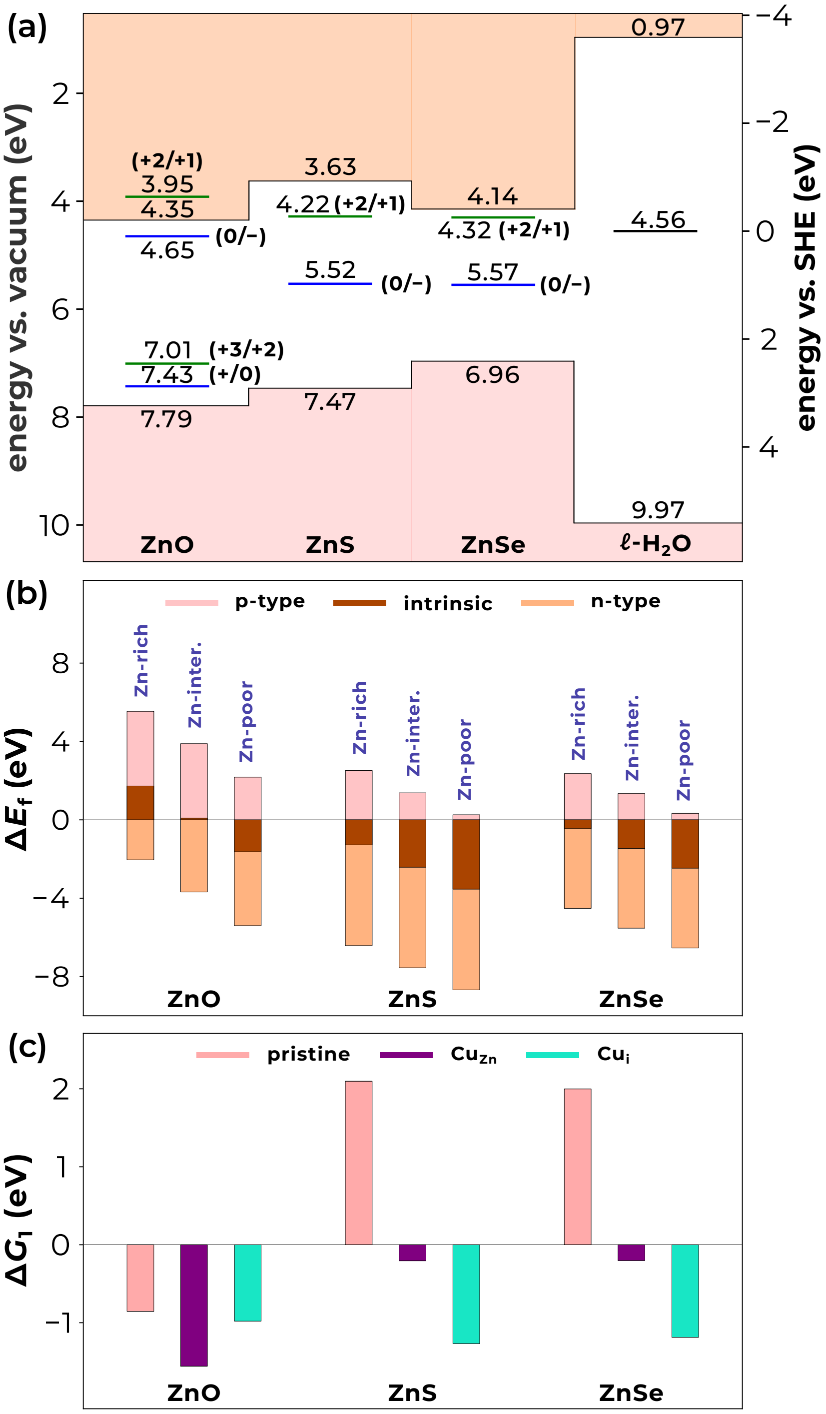

Figure 4. (**a**) Adiabatic charge transition levels of substitutional and interstitial Cu at the $(10\bar{1}0)$ surface of ZnO and at the (110) surface of ZnS and ZnSe. Levels associated with the substitutional (interstitial) Cu defect are represented by blue (green) horizontal lines. Band edges of ZnO, ZnS, and ZnSe, corresponding for each material to the respective experimental value [103,104], are aligned with respect to the vacuum level and then referred to the standard hydrogen electrode via the alignment proposed in refs. [98,108]. (**b**) Calculated values of ΔE_f (cf. main text for definition) for different materials surfaces under different growth conditions and considering *p*-type, intrinsic, and *n*-type samples. Negative (positive) values indicate that the surface substitutional (interstitial) Cu is more stable. Data from ref. [43] are analysed for ZnO. (**c**) ΔG_1 of the HER, as calculated from electronic-structure calculations on pristine and doped slabs of ZnO, ZnS, and ZnSe.

When considering the alignment of the calculated defects' energy levels with the H^+/H_2 redox potential [cf. Figure 4b], it is noted that, for ZnO, the $(0/-1)$ level of Cu_{Zn} is favourably placed with respect to the H^+/H_2 reduction level [43]. This is not the case for ZnS and ZnSe, for which the $(0/-1)$ CTL is observed to lie more than 1 eV below the H^+/H_2 potential, a result which would imply a substantial energy barrier for electron transfer. Differently, Cu_i (+2/+) levels are found to be suitably placed, as they are found at 0.24 and 0.34 eV above the H^+/H_2 redox level for ZnS and ZnSe, respectively. However, defect formation energies indicate that interstitials might be far less abundant on ZnS and ZnSe surfaces. Moreover, the available experimental data suggest a more marked effect of Cu doping on the photocatalytic efficiencies of ZnS [54–57] , which cannot be truly rationalised in terms of the calculated defect energy levels. Overall, while charge transition levels may provide hints at defect-mediated photocatalytic activity, understanding its genuine mechanism, which could differ from those usually proposed for metal catalysts [109,110], deserves further investigation.

Therefore, this issue is examined in greater detail by modelling the energetics and the mechanism of HER. To this end, the overpotential of the reaction is first calculated using the CHE. In detail, both the pristine slabs and those bearing a surface Cu defect (either substitutional or interstitial) are considered for all the investigated materials. When calculating $\mu[H^*_{ads}]$ in Equation (12), adsorption of H is evaluated on X and Zn surface site for pristine slabs, and adsorption on X, Zn and on the surface Cu defect for the doped slabs. The total energy of the most stable structural configuration is then included in Equation (12). Computations on the slabs with surface Cu^q_{Zn} are initiated from $q = 0$, while $q = +2$ is considered for Cu_{Zn}, i.e., d^9 Cu(II) in both cases. The calculated values of ΔG_1 are given in Figure 4c for pristine and doped slabs. First, the performance of the pristine materials is discussed. For ZnO, $\Delta G_1 = -0.85$ eV and, hence, $\eta_{HER} = 0.85$ V are computed, meaning that the reaction is hindered by the strong interaction between the surface and the adsorbate, making the second step of the mechanism decidedly uphill. An opposite situation is observed for ZnS and ZnSe: ΔG_1 values exceeding 2 eV result in likewise dramatic overpotentials. Therefore, in this case, the limiting step of the reaction is given by poor H adsorption. This is consistent with the reduced electronegativity of S and Se, if compared with O at the surface of the oxide, resulting in weaker surface-adsorbate interactions. When moving to the doped systems, surprisingly, ΔG_1 (and hence η_{HER}) is observed to substantially rise from 0.85 up to 1.55 eV when comparing pristine and Cu_{Zn}-bearing ZnO slab. In stark contrast, both ZnS and ZnSe see a sizeable stabilisation in the adsorbate when a surface Cu_{Zn} is present at the surface. This lowers ΔG_1 and hence brings to overpotentials reduced by as much as 2 V. Finally, the overpotential remains substantial for all the materials (above 1 eV) for the reaction occurring at the interstitial site and is again determined by the second step of the reaction, i.e., H_2 formation and desorption. Therefore, the present analysis reveals that the dopant generally enhances the stability of the adsorbate+slab system. However, H is already bound too strongly on the pristine ZnO surface and, hence, the increased stability due to Cu entails a higher value of η_{HER}. On the other hand, H is poorly adsorbed on both the pristine surfaces of ZnS and ZnSe ($\Delta G_1 > 2$ eV), and the Cu-induced stabilisation, in the case of substitutional defect, brings ΔG_1 very close to zero, i.e., the sweet spot for HER as formulated by the Sabatier principle. Refs. [71,111,112] For comparison, optimal co-catalysts in state-of-the-art photocatalytic systems give effective overpotentials on the order of 0.1–0.3 V [71].

To understand the origin of such a large effect on ΔG_1 and, hence, on η_{HER}, the structural and electronic features of the adsorbates on the slab are investigated. The pristine materials are first discussed, with the most stable structures being depicted in Figure 5a. In ZnO, the lowest-energy structure features a proton adsorbed on an undercoordinated surface O, while the extra electron is assimilated in a delocalised CBM state. This is motivated by the strong ionic character of the O-H bond, which impedes reduction. Oppositely, radical $H^{\cdot}$ is preferentially formed on a Zn surface site for ZnS and ZnSe, see Section S6 for the relative stability of different adsorption sites. The computed spin densities, strongly localised on H, confirm the radical nature of the adsorbate.

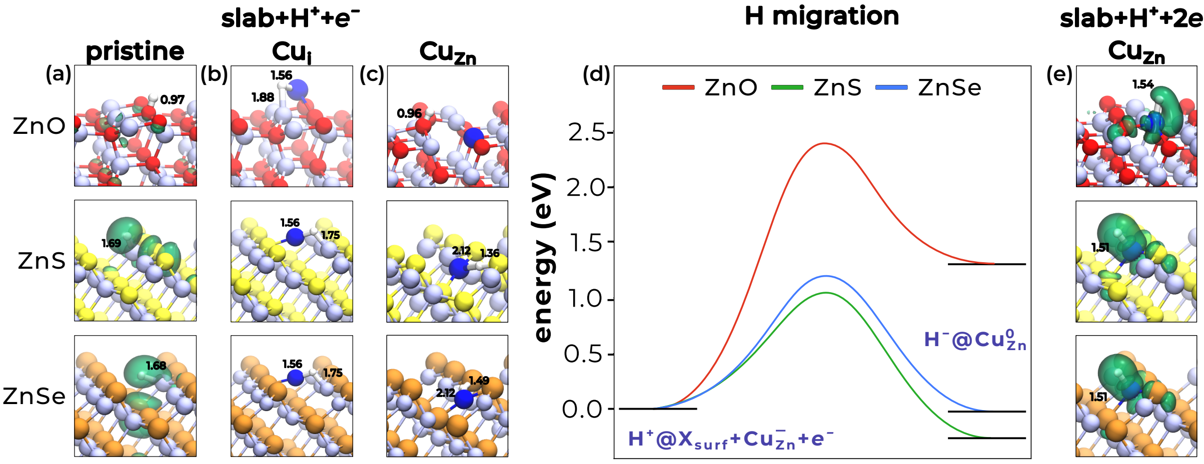

Figure 5. Stick and ball representation of the most stable structural configurations for slabs of zinc chalcogenides with an extra proton and electron. Panel (**a**) for pristine slabs, (**b**) for surface Cu_i, (**c**) for surface Cu_{Zn}. (**d**) energy profile for H migration from a surface chalcogen site to a Cu, as calculated from linear transit simulations. For each chalcogenide, energies are referred to that of the initial state. (**e**) Stick and ball representation of the most stable structural configurations for Cu_{Zn}-bearing slabs with an extra proton and two electrons, entailing the formation of a surface hydride (cf. main text). H atom is portrayed in white, Zn in grey, Cu in blue, S in yellow, and Se in orange. Lengths of the bonds involving the adsorbate are also reported (in Å). Isodensity representations of the spin density (isovalue = 0.001) are shown in green, when appropriate.

In doped slabs, the chemisorption of H is found to be completely changed: the addition of H^+ and e^- to Cu_i results in the adsorbate bridging the Cu dopant and a lattice Zn, see Figure 5b. However, such strong interactions over-stabilise the adsorbate, resulting in highly negative ΔG_1 values, corresponding to overpotentials above 1 V. More interestingly, upon the substitution of a surface Zn with a Cu, the adsorbate binds preferentially to a surface, X, close to the dopant in all the chalcogenides, while displaying strong interactions with the neighbouring Cu. These are evidenced by remarkable surface reconstruction bringing the two ions together; see Figure 5b; In particular, Cu-H distances of ≈2.8 Å are recorded for ZnO and as small as ≈2.1 Å for ZnS and ZnSe. Furthermore, no spin localisation is envisaged. These observations distinctly indicate that such a structural configuration does not correspond to radical $H^{\cdot}$ but coincides with a strongly interacting couple formed by adsorbed H^+ and reduced Cu^-_{Zn}. This is also confirmed by inspection of the doped slabs bearing only an adsorbed H^+ on a surface X, in which such interactions are absent (see Section S7 in SI), signifying that the reduction in the defect, upon capture of an electron, is at the root of the remarkable energy gain with respect to pristine systems.

The present results achieved for Cu_{Zn}, which are decidedly promising for ZnS and ZnSe, call for a further inspection of the reaction mechanism. In fact, while giving low ΔG_1, the product of the reaction does *not* correspond to radical $H^{\cdot}$, as envisaged by the standard HER mechanism. Therefore, it remains unclear how H_2 can be produced, given that the photo-generated electron is captured by the dopant, consistently with the position of the energy levels presented in Figure 4a. In particular, it is considered whether the addition of a second electron, which is possible under photocharging conditions, may allow the formation of a reduced H species. Interestingly, when carrying out calculations on slab with an extra H^+ and *two* electrons, two possible energy minima are obtained, with the adsorbate bound (i) to surface X [very similar to the structures shown in Figure 5c] and (ii) to $\mathrm{Cu_{Zn}}$, on which it forms a hydride. In the latter case, spin localisation also suggests the defect has reverted back to d^9 Cu(II) typical of $\mathrm{Cu^0_{Zn}}$; see Figure 5e. Notably, for ZnO, formation of the hydride is strongly disfavoured by as much as 0.60 eV, while it is a favourite for ZnS and ZnSe, for which the surface H^- is found to be slightly more stable by 0.60 and 0.30 eV, respectively. Furthermore, the migration of the adsorbate from surface X to Cu implies the crossing of an energy barrier, which is here estimated, via the linear transit method, to be 0.9, 0.41, and 0.28 eV for ZnO, ZnS, and ZnSe, respectively; see Figure 5d. Including the zero-point energy (ZPE) of the adsorbed hydrogen in the initial state (cf. Section S2 of the SI) substantially modifies the effective activation barriers. Subtracting the harmonic ZPE contribution (0.41, 0.30, and 0.17 eV for ZnO, ZnS, and ZnSe, respectively) yields residual barriers of 0.49 eV for ZnO and only ≈0.11 eV for ZnS and ZnSe. At room temperature, the latter corresponds to thermally accessible activation energies, whereas in ZnO proton migration remains strongly kinetically hindered. These results indicate that Cu substitution renders hydride formation on ZnS and ZnSe dynamically viable under photocatalytic conditions, while the stronger H–O interaction in ZnO further worsen the kinetics of the HER reaction.

Overall, in virtue of the comprehensive *ab initio* investigation presented so far, the following mechanism for the global HER reaction on Cu-doped ZnX is proposed, as schematised in Figure 6, and consisting of the following steps:

- A reduction in the surface substitutional Cu operated by a photogenerated electron:

$$\mathrm{Cu^0_{Zn}} + e^- \rightarrow \mathrm{Cu^-_{Zn}}, \tag{17}$$

  which takes place, as the acceptor level is within the band gap of each material.
- adsorption of H^+ on a surface X site close to the defect:

$$\mathrm{H^+(aq)} + \mathrm{X_{surf}} \rightarrow \mathrm{H^+_{ads}@X_{surf}}. \tag{18}$$

  It is noted that, in the case of ZnO, this step is expected to occur already *before* Cu reduction, as protons are likely to be adsorbed in appreciable concentration on the charge-neutral surface (see Refs. [113,114]). For ZnS and ZnSe, which are far less reactive, as indicated by the highly positive $\Delta G1$ values of the pristine slabs, adsorption of protons is prompted by strong interactions with the reduced surface defect.
- Upon the injection of a second electron, the adsorbate can migrate towards the defect site, which is concomitantly oxidated:

$$\mathrm{H^+_{ads}@X_{surf}} + \mathrm{Cu^-_{Zn}} + e^- \rightarrow \mathrm{H^-_{ads}@Cu^0_{Zn}} + \mathrm{X_{surf}}. \tag{19}$$

  This reaction step is expected to be endothermic on the $(10\bar{1}0)$ surface of ZnO and exothermic on the (110) surfaces of ZnS and ZnSe. It is argued that the faster completion of this reaction step, as evidenced by the lower energy barrier associated with it, is at the root of the superior performances registered experimentally for Cu-enriched ZnS, with respect to the doped oxide.
- H_2 is produced by a swift reaction between surface hydride and aqueous protons and then migrates from the electrode to the gas-phase.

$$\mathrm{H^-_{ads}@Cu^0_{Zn}} + \mathrm{H^+(aq)} \rightarrow \mathrm{H_2(g)} + \mathrm{Cu^0_{Zn}}. \tag{20}$$

  This step, which frees the surface Cu to initiate another reaction cycle, is associated with the residual overpotential (below 0.2 V) of the reaction on Cu-doped ZnS and ZnSe.

Finally, it is noted that the proposed reaction mechanism is equivalent if it is initiated from $\mathrm{Cu}_{\mathrm{Zn}}^{-}$, i.e., if the Fermi level of the material lies close to the CBM, and hence, the defect is already in its reduced form under charge-neutral conditions [see Figure 4a]. In such a case, the cycle is simply shifted by one step, and hence, it is prompted by adsorption of protons near the defect site and closed by a photogenerated electron restoring $\mathrm{Cu}_{\mathrm{Zn}}^{-}$, cf. Figure 6.

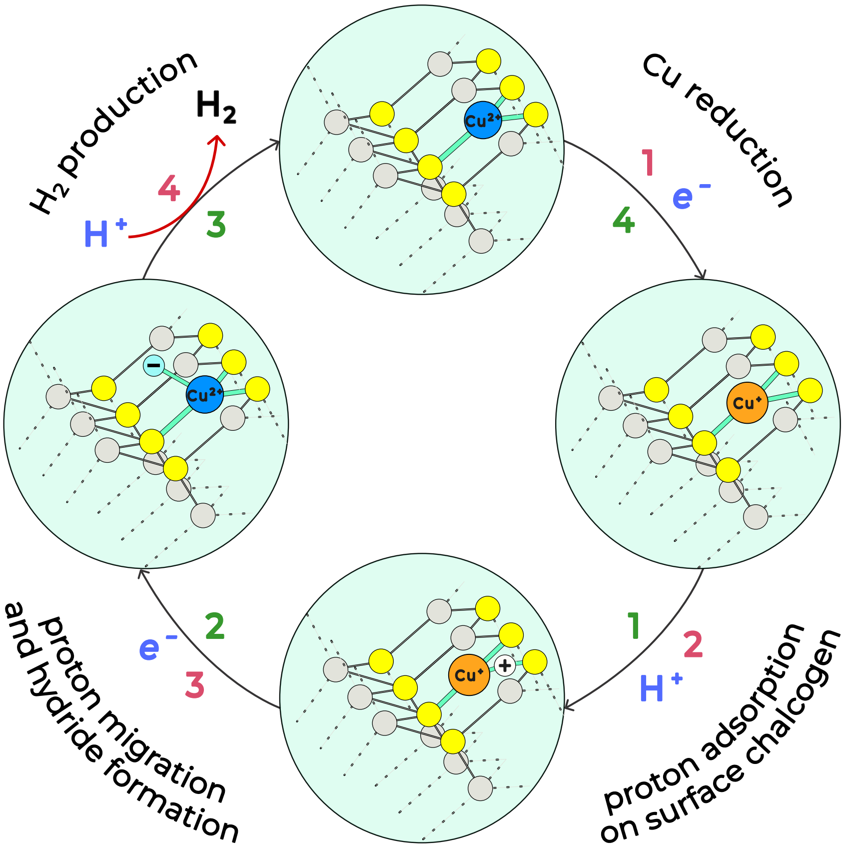

Figure 6. Schematic representation of the proposed HER mechanism on zinc chalcogenides' surfaces bearing a surface $\mathrm{Cu}_{\mathrm{Zn}}$. Red (green) numbers indicate the sequence of steps for $\mathrm{Cu}_{\mathrm{Zn}}^{0}$ ($\mathrm{Cu}_{\mathrm{Zn}}^{-}$).

5. Conclusions

In this work, a comprehensive and comparative first-principles investigation of Cu defects in ZnO, ZnS, and ZnSe has been presented, addressing their bulk and surface energetics, electronic structure, optical signatures, and role in the hydrogen evolution reaction. By combining a rigorous grand-canonical treatment of charged defects with hybrid DFT calculations and the CHE approach, a unified microscopic picture of Cu doping across the ZnX chalcogenide series has been provided. The results revealed a clear qualitative distinction between ZnO and the heavier chalcogenides. While ZnO supports both donor- and acceptor-like Cu defects and exhibits strong electron–lattice coupling with pronounced Jahn–Teller distortions, ZnS and ZnSe display a markedly different defect physics. In these materials, substitutional $\mathrm{Cu}_{\mathrm{Zn}}$ behaves as a mid-gap acceptor with similar absolute charge-transition levels in both hosts, whereas interstitial Cu is electrically inactive in the bulk. The reduced ionicity and enhanced covalency of ZnS and ZnSe suppress hole localisation and stabilise electron trapping, leading to a crossover in carrier localisation along the series. At the surface, defect energetics and charge-transition levels undergo substantial shifts with respect to the bulk, profoundly impacting photocatalytic behaviour. It is found that surface substitutional Cu is the key electronically active defect for ZnS and ZnSe under realistic conditions, while interstitial Cu may become stabilised only in specific regimes. The alignment of defect levels with the H^+/H_2 redox potential has suggested a defect-mediated boost of photocatalytic activity but was found to be insufficient to rationalise the experimentally observed trends.

The explicit modelling of the HER mechanism revealed the microscopic origin of the markedly different catalytic responses by invoking defect-mediated mechanism in which photogenerated electrons are first trapped at Cu_{Zn}, followed by a cooperative interaction between the reduced defect and adsorbed protons, ultimately enabling hydride formation and H_2 evolution. The calculations showed that Cu substitution in ZnS and ZnSe simultaneously fulfils both the criteria for optimal HER activity, i.e., hydrogen adsorption free energies close to thermoneutral conditions, together with kinetically accessible reaction pathways. In fact, in these materials, the Cu site was found to tune the hydrogen adsorption toward the Sabatier optimum, while the exiguous energy barrier for H migration renders hydride formation thermally accessible at ambient conditions. In contrast, in ZnO the stronger H–O interaction leaves a residual barrier of 0.49 eV, kinetically hindering transfer to the Cu site, and thus limiting catalytic turnover.

More broadly, the findings demonstrated that the catalytic impact of doping can be envisaged from band alignment considerations, but the accurate determination of defect thermodynamics, charge localisation, and surface reaction energetics is required to rationalise experimental trends. The present study establishes defect engineering as a powerful tool to tune hydrogen adsorption thermodynamics in wide band-gap chalcogenides and provides design principles for optimising Cu-doped ZnX materials for photocatalytic applications. The natural continuation of the present study will extend the employed methodology to different systems and photocatalytic reactions, as well as performing simulations of complete semiconductor water interfaces to study the reaction mechanism under realistic conditions.

Supplementary Materials: The following supporting information can be downloaded at: https://www.mdpi.com/article/10.3390/nanoenergyadv6020017/s1, Electronic Supplementary Information includes additional analysis of the data. Section S1 provides the theoretical framework for the evaluation of chemical potentials of constituent elements of ZnS, ZnSe, and the Cu dopant, as well as the calculated enthalpies of formation for ZnS, ZnSe and the competing phases considered. Section S2 supplies the energy correction terms outlined in Equation (15) and the calculated vibrational frequencies for adsorbed $H^{\cdot}$ on both pristine and doped materials. Section S3 provides the structural parameters employed for the modelling of both the bulk and slab materials, as well as their energy gaps and the calculated electrostatic potentials for the surfaces. Sections S4 and S5 delve into the structural and electronic properties of the Cu-doped ZnS and ZnSe bulk and (110) slabs, respectively. Section S6 provides the energetics of the $H^{\cdot}$ adsorption on the pristine surfaces of Zn chalcogenides, and Section S7 outlines the H^+ adsorption on the Cu-doped ZnX surfaces. Additional refs. [115–127].

Author Contributions: M.L.: formal analysis, investigation, data curation, writing—original draft preparation, and visualisation. F.A.: conceptualisation, methodology, validation, resources, writing—review and editing, supervision, project administration, and funding acquisition. All authors have read and agreed to the published version of the manuscript.

Funding: This research was funded by PRIN 2022-PNRR grant (P2022W9773).

Data Availability Statement: All the relevant data (inputs, outputs) used to produce the computational results presented in this work are available at the following public repository: https://github.com/Michi12Michi/Cu-ZnX-Supporting-data (accessed on 28 April 2026).

Acknowledgments: F.A. and M.L. thankfully acknowledge PRIN 2022-PNRR grant (P2022W9773) for funding. The authors also acknowledge the CINECA award under the ISCRA initiative, for the availability of high-performance computing resources: projects MHP-DEF (HP10CNQAEA), Photofix (HP10C2S6ML) and PAWS-ZnX (HP10CTDQYG).

Conflicts of Interest: The authors declare no conflicts of interest.

References

1. Sharma, D.K.; Shukla, S.; Sharma, K.K.; Kumar, V. A review on ZnO: Fundamental properties and applications. *Mater. Today Proc.* **2022**, *49*, 3028–3035. [CrossRef]
2. Chakrabarti, A.; Alessandri, E. Syntheses, properties, and applications of ZnS-based nanomaterials. *Appl. Nano* **2024**, *5*, 116–142. [CrossRef]
3. Zhang, Q.; Li, H.; Ma, Y.; Zhai, T. ZnSe nanostructures: Synthesis, properties and applications. *Prog. Mater. Sci.* **2016**, *83*, 472–535. [CrossRef]
4. Chatterjee, A.; Kumar, G.K.; Roymahapatra, G.; Das, H.S.; Jaishree, G.; Rao, T.S. Zinc chalcogenide nanostructures: Synthesis methodologies and applications—A review. *Front. Nanotechnol.* **2024**, *6*, 1433591. [CrossRef]
5. Fu, H. Environmentally friendly and earth-abundant colloidal chalcogenide nanocrystals for photovoltaic applications. *J. Mater. Chem. C* **2018**, *6*, 414–445. [CrossRef]
6. Li, P.; He, T. Recent advances in zinc chalcogenide-based nanocatalysts for photocatalytic reduction of CO_2. *J. Mater. Chem. A* **2021**, *9*, 23364–23381. [CrossRef]
7. Aldemir, C.H.; Yazici, A.F.; Ergezer, N.; Korkmaz, T.C.; Mutlugun, E.; Kelestemur, Y. Zinc Chalcogenide Based Shell Layers for Colloidal Quantum Wells. *Adv. Mater. Interfaces* **2025**, *12*, 2500120. [CrossRef]
8. Shen, C.; Yin, Z.; Collins, F.; Pinna, N. Atomic Layer Deposition of Metal Oxides and Chalcogenides for High Performance Transistors. *Adv. Sci.* **2022**, *9*, 2104599. [CrossRef] [PubMed]
9. Shen, H.; Yuan, X.; Ren, Y.; Huang, Z.; Zhu, H.; Zhang, S.; Wang, Y. Origin of Efficient and Tunable Dual-Band Emission From Zinc Chalcogenide Quantum Dots for Sustainable Photonics. *Laser Photonics Rev.* **2025**, *19*, 2400610. [CrossRef]
10. Chiu, M.Y.; Chen, C.C.; Sheu, J.T.; Wei, K.H. An optical programming/electrical erasing memory device: Organic thin film transistors incorporating core/shell CdSe@ZnSe quantum dots and poly (3-hexylthiophene). *Org. Electron.* **2009**, *10*, 769–774. [CrossRef]
11. Hussain, S.; Yang, X.; Yang, J.; Li, Q. Theoretical insights into the mechanism of photocatalytic reduction of CO_2 and water splitting over II-VI zinc chalcogenide semiconductor. *Mater. Today Sustain.* **2024**, *25*, 100686. [CrossRef]
12. Chen, S.; Li, C.; Domen, K.; Zhang, F. Particulate metal chalcogenides for photocatalytic Z-scheme overall water splitting. *Joule* **2023**, *7*, 2445–2467. [CrossRef]
13. Du, K.; Lang, X.; Yang, Y.; Cheng, C.; Lan, N.; Qiu, K.; Mao, J.; Wang, W.; Ling, T. Hydrogen-assisted activation of N_2 molecules on atomic steps of ZnSe nanorods. *Nano Res.* **2023**, *16*, 6721–6727. [CrossRef]
14. Li, J.; Wang, J.; Wang, G.; Zhao, S.; Yang, Z.; Wang, X.; Yan, Y. CeO_2/ZnO heterojunction as efficient catalyst for electrocatalytic nitrogen reduction reaction via an "electron pump" effect. *J. Rare Earths* **2025**, *44*, 698–703. [CrossRef]
15. Baranowska-Korczyc, A.; Kościński, M.; Coy, E.L.; Grześkowiak, B.F.; Jasiurkowska-Delaporte, M.; Peplińska, B.; Jurga, S. ZnS coating for enhanced environmental stability and improved properties of ZnO thin films. *RSC Adv.* **2018**, *8*, 24411–24421. [CrossRef] [PubMed]
16. Butola, D.; Purohit, L. Exceptional stability and reusability of Cu-doped ZnO:SnO_2 nanocomposites for photocatalysis under visible light. *Mater. Chem. Phys.* **2024**, *328*, 130021. [CrossRef]
17. Gao, Z.; Banerjee, P. Review Article: Atomic layer deposition of doped ZnO films. *J. Vac. Sci. Technol. A* **2019**, *37*, 050802. [CrossRef]
18. Verduzco, A.C.; Aguilar, J.U.B.; Huitrón, J.C.A. Photoluminescence and electroluminescence properties of Cu-doped ZnS thin films fabricated by ultrasonic spray pyrolysis. *J. Alloys Compd.* **2025**, *1022*, 179834. [CrossRef]
19. Kim, J.Y.; Yang, J.; Yu, J.H.; Baek, W.; Lee, C.H.; Son, H.J.; Hyeon, T.; Ko, M.J. Highly Efficient Copper–Indium–Selenide Quantum Dot Solar Cells: Suppression of Carrier Recombination by Controlled ZnS Overlayers. *ACS Nano* **2015**, *9*, 11286–11295. [CrossRef]
20. Woo, M.Y.; Choi, K.; Lee, J.H.; Park, S.Y.; Noh, J.H. Recent Progress in the Semiconducting Oxide Overlayer for Halide Perovskite Solar Cells. *Adv. Energy Mater.* **2021**, *11*, 2003119. [CrossRef]
21. Wang, Y.; Zhong, M.; Wang, W.; Wang, Q.; Wu, W.; Luo, X. Effects of ZnSe modification on the perovskite films and perovskite solar cells based on ZnO nanorod arrays. *Appl. Surf. Sci.* **2019**, *495*, 143552. [CrossRef]
22. Xu, X.; Li, S.; Chen, J.; Cai, S.; Long, Z.; Fang, X. Design principles and material engineering of ZnS for optoelectronic devices and catalysis. *Adv. Funct. Mater.* **2018**, *28*, 1802029. [CrossRef]
23. Demontis, V.; Isram, M.; Abbas Khan, N.; Amin, N.; Mahmood, K.; Rossella, F. ZnSe nanoparticles for thermoelectrics: Impact of Cu-doping. *Crystals* **2023**, *13*, 695. [CrossRef]
24. Pereira, L.F.; Ferreira, W.L.; Correa, B.S.; Costa, M.S.; Costa, C.S.; Filho, A.A.; Sales, T.S.; Bosch-Santos, B.; Schell, J.; Burimova, A.; et al. Cobalt Doping Effects in Zinc Oxide: A Combined Experimental and Ab Initio Approach. *Crystals* **2023**, *14*, 51. [CrossRef]
25. Sun, R.; Jing, B.; Zhang, Y.; Li, J.; Zhou, Y.; Song, C.; Wang, D. Adjusting the wide bandgaps of $In(OH)_3$ and ZnS by S and In doping for applications at visible-light photocatalytic hydrogen evolution. *Int. J. Hydrogen Energy* **2025**, *127*, 202–212. [CrossRef]

26. Al-Kuhaili, M.; Dastageer, M. Enhanced conductivity, photoresponse, and band-gap tuning of ZnSe thin films doped with In, Sn, and Sb. *Surf. Interfaces* **2025**, *80*, 108226. [CrossRef]
27. Lee, G.J.; Anandan, S.; Masten, S.J.; Wu, J.J. Photocatalytic hydrogen evolution from water splitting using Cu doped ZnS microspheres under visible light irradiation. *Renew. Energy* **2016**, *89*, 18–26. [CrossRef]
28. Li, M.; Tu, X.; Wang, Y.; Su, Y.; Hu, J.; Cai, B.; Lu, J.; Yang, Z.; Zhang, Y. Highly Enhanced Visible-light-driven Photoelectrochemical Performance of ZnO-modified In_2S_3 Nanosheet Arrays by Atomic Layer Deposition. *Nano-Micro Lett.* **2018**, *10*, 45. [CrossRef]
29. Dingle, R. Luminescent Transitions Associated with Divalent Copper Impurities and the Green Emission from Semiconducting Zinc Oxide. *Phys. Rev. Lett.* **1969**, *23*, 579. [CrossRef]
30. Yan, Y.; Al-Jassim, M.; Wei, S.H. Doping of ZnO by Group-IB Elements. *Appl. Phys. Lett.* **2006**, *89*, 181912. [CrossRef]
31. Yang, Y.; Zhang, P.; Yang, J.; Wei, S.H. Chemical Trend of a Cu Impurity in Zn Chalcogenides. *Phys. Rev. B* **2020**, *101*, 174101. [CrossRef]
32. Tawfik, W.Z.; Farghali, A.; Moneim, A.; Imam, N.; El-Dek, S. Outstanding features of Cu-doped ZnS nanoclusters. *Nanotechnology* **2018**, *29*, 215709. [CrossRef]
33. Priyadarshini, P.; Das, S.; Naik, R. A review on metal-doped chalcogenide films and their effect on various optoelectronic properties for different applications. *RSC Adv.* **2022**, *12*, 9599–9620. [CrossRef] [PubMed]
34. Chadi, D. The problem of doping in II-VI semiconductors. *Annu. Rev. Mater. Sci.* **1994**, *24*, 45–62. [CrossRef]
35. Desnica, U. Doping limits in II-VI compounds—Challenges, problems and solutions. *Prog. Cryst. Growth Charact. Mater.* **1998**, *36*, 291–357. [CrossRef]
36. Ortíz-Ramos, D.E.; González, L.A.; Ramirez-Bon, R. p-Type transparent Cu doped ZnS thin films by the chemical bath deposition method. *Mater. Lett.* **2014**, *124*, 267–270. [CrossRef]
37. Orita, M.; Narushima, T.; Yanagita, H. Transparent conductive Cu-doped ZnSe film deposited at room temperature using compound sources followed by laser annealing. *Jpn. J. Appl. Phys.* **2007**, *46*, L976. [CrossRef]
38. Dietz, R.; Kamimura, H.; Sturge, M.; Yariv, A. Electronic Structure of Copper Impurities in ZnO. *Phys. Rev.* **1963**, *132*, 1559. [CrossRef]
39. Lyons, J.; Alkauskas, A.; Janotti, A.; Van de Walle, C. Deep Donor State of the Copper Acceptor as a Source of Green Luminescence in ZnO. *Appl. Phys. Lett.* **2017**, *111*, 042101. [CrossRef]
40. Gallino, F.; Di Valentin, C. Copper Impurities in Bulk ZnO: A Hybrid Density Functional Study. *J. Chem. Phys.* **2011**, *134*, 144506. [CrossRef]
41. Peng, W.; Cong, G.; Qu, S.; Wang, Z. Synthesis and photoluminescence of ZnS:Cu nanoparticles. *Opt. Mater.* **2006**, *29*, 313–317. [CrossRef]
42. Suyver, J.; Van der Beek, T.; Wuister, S.; Kelly, J.; Meijerink, A. Luminescence of nanocrystalline ZnSe:Cu. *Appl. Phys. Lett.* **2001**, *79*, 4222–4224. [CrossRef]
43. Loriso, M.; Ambrosio, F. From Bulk to Surface: A First-Principles Study of Cu Doping in ZnO and Its Implications for Photocatalysis. *Energy Fuels* **2026**, *40*, 3397–3407. [CrossRef]
44. Hoang, K.; Latouche, C.; Jobic, S. Defect energy levels and persistent luminescence in Cu-doped ZnS. *Comput. Mater. Sci.* **2019**, *163*, 63–67. [CrossRef]
45. Thompson, S.M.; Sahin, C.; Yang, S.; Flatté, M.E.; Murray, C.B.; Bassett, L.C.; Kagan, C.R. Red emission from copper-vacancy color centers in zinc sulfide colloidal nanocrystals. *ACS Nano* **2023**, *17*, 5963–5973. [CrossRef] [PubMed]
46. Vaiano, V.; Iervolino, G. Photocatalytic Hydrogen Production from Glycerol Aqueous Solution Using Cu-Doped ZnO under Visible Light Irradiation. *Appl. Sci.* **2019**, *9*, 2741. [CrossRef]
47. Karthik, T.; Maldonado, A.; Olvera, M.d.l.L.; Hernández, A.; Vega-Pérez, J.; Gómez-Pozos, H. Copper-doped ZnO Thin Films Deposited by Spray Pyrolysis: Effect of Water Content in Starting Solution on Methylene Blue Degradation by Photocatalysis. *J. Electron. Mater.* **2021**, *50*, 5542–5552. [CrossRef]
48. Javed, M.; Qamar, M.A.; Shahid, S.; Alsaab, H.O.; Asif, S. Highly Efficient Visible Light Active Cu–ZnO/SgC_3N_4 Nanocomposites for Efficient Photocatalytic Degradation of Organic Pollutants. *RSC Adv.* **2021**, *11*, 37254–37267. [CrossRef]
49. Manzoor, M.F.; Ahmed, E.; Ahmad, M.; Ahmad, I.; Rana, A.M.; Ali, A.; Ghouri, M.I.; Manzoor, M.S.; Aziz, M.T. Enhanced Photocatalytic Activity of Hydrogen Evolution through Cu Incorporated ZnO Nano Composites. *Mater. Sci. Semicond. Process.* **2020**, *120*, 105278. [CrossRef]
50. Khumphon, J.; Ahmed, R.; Imboon, T.; Giri, J.; Chattham, N.; Mohammad, F.; Kityakarn, S.; Mangala Gowri, V.; Thongmee, S. Boosting Photocatalytic Activity in Rhodamine B Degradation Using Cu-Doped ZnO Nanoflakes. *ACS Omega* **2025**, *10*, 9337–9350. [CrossRef]
51. Hao, Z.; Hu, M.; Kang, Z.; Wang, J.; Liu, C.; Feng, Q.; Xu, L. Cu modified ZnS photocatalysts for enhancing the photocatalytic H_2 production activity. *Int. J. Hydrogen Energy* **2025**, *106*, 403–410. [CrossRef]

52. Daskalakis, I.; Vamvasakis, I.; Papadas, I.T.; Tsatsos, S.; Choulis, S.A.; Kennou, S.; Armatas, G.S. Surface defect engineering of mesoporous Cu/ZnS nanocrystal-linked networks for improved visible-light photocatalytic hydrogen production. *Inorg. Chem. Front.* **2020**, *7*, 4687–4700. [CrossRef]
53. Soleymani, A.R.; Souri, D.; Nezhad, E.M.; Khezripour, A.R. Evaluation of photocatalytic activity of ZnSe: Cu nanoparticles: Synthesis, experimental measurement, kinetic study, and ANN modeling. *Results Eng.* **2026**, *29*, 108960. [CrossRef]
54. Lee, G.J.; Chen, H.C.; Wu, J.J. (In, Cu) Co-doped ZnS nanoparticles for photoelectrochemical hydrogen production. *Int. J. Hydrogen Energy* **2019**, *44*, 110–117. [CrossRef]
55. Bao, L.; Ali, S.; Dai, C.; Zeng, Q.; Zeng, C.; Jia, Y.; Liu, X.; Wang, P.; Ren, X.; Yang, T.; et al. A full-spectrum ZnS photocatalyst with gradient distribution of atomic copper dopants and concomitant sulfur vacancies for highly efficient hydrogen evolution. *ACS Nano* **2024**, *18*, 5878–5889. [CrossRef]
56. Li, Z.; Wang, Y.; Choy, K.L. Eco-Friendly Solar-Powered H_2 Generation from Plastic Waste Using Earth-Abundant Cu-Doped ZnS Catalysts. *Nanomaterials* **2025**, *15*, 1311. [CrossRef]
57. Liu, Q.; Luan, W.; Zhang, X.; Zhao, R.; Han, J.; Wang, L. $NiMoP_2$ co-catalyst modified Cu doped ZnS for enhanced photocatalytic hydrogen evolution. *Sep. Purif. Technol.* **2025**, *354*, 128666. [CrossRef]
58. Freysoldt, C.; Neugebauer, J.; Van de Walle, C.G. Fully *Ab Initio* Finite-Size Corrections for Charged-Defect Supercell Calculations. *Phys. Rev. Lett.* **2009**, *102*, 016402. [CrossRef]
59. Komsa, H.P.; Rantala, T.T.; Pasquarello, A. Finite-Size Supercell Correction Schemes for Charged Defect Calculations. *Phys. Rev. B* **2012**, *86*, 045112. [CrossRef]
60. Ambrosio, F.; Chen, W.; Pasquarello, A. Electronic Energy Levels of Aqueous Hydroxyl Species. *Phys. Chem. Chem. Phys.* **2025**, *27*, 23079–23090. [CrossRef]
61. Falletta, S.; Wiktor, J.; Pasquarello, A. Finite-size Corrections of Defect Energy Levels Involving Ionic Polarization. *Phys. Rev. B* **2020**, *102*, 041115. [CrossRef]
62. Verma, A. High frequency and static dielectric constants of zinc blende structured solids. *Solid State Commun.* **2011**, *151*, 1945–1948. [CrossRef]
63. Komsa, H.P.; Pasquarello, A. Finite-size Supercell Correction for Charged Defects at Surfaces and Interfaces. *Phys. Rev. Lett.* **2013**, *110*, 095505. [CrossRef]
64. Rossmeisl, J.; Qu, Z.W.; Zhu, H.; Kroes, G.J.; Nørskov, J. Electrolysis of water on oxide surfaces. *J. Electroanal. Chem.* **2007**, *607*, 83–89. [CrossRef]
65. Nørskov, J.K.; Rossmeisl, J.; Logadottir, A.; Lindqvist, L.; Kitchin, J.R.; Bligaard, T.; Jónsson, H. Origin of the Overpotential for Oxygen Reduction at a Fuel-Cell Cathode. *J. Phys. Chem. B* **2004**, *108*, 17886–17892. [CrossRef]
66. Kulkarni, A.; Siahrostami, S.; Patel, A.; Nørskov, J.K. Understanding Catalytic Activity Trends in the Oxygen Reduction Reaction. *Chem. Rev.* **2018**, *118*, 2302–2312. [CrossRef]
67. Guo, X.; Gu, J.; Lin, S.; Zhang, S.; Chen, Z.; Huang, S. Tackling the Activity and Selectivity Challenges of Electrocatalysts toward the Nitrogen Reduction Reaction via Atomically Dispersed Biatom Catalysts. *J. Am. Chem. Soc.* **2020**, *142*, 5709–5721. [CrossRef]
68. Li, H.; Reuter, K. Active-Site Computational Screening: Role of Structural and Compositional Diversity for the Electrochemical CO_2 Reduction at Mo Carbide Catalysts. *ACS Catal.* **2020**, *10*, 11814–11821. [CrossRef]
69. Liang, Q.; Ouhbi, H.; Österbacka, N.; Ambrosio, F.; Wiktor, J. Defect engineering in $BiVO_4$ photoanodes: The synergistic role of nitrogen doping and oxygen vacancy for oxygen evolution reaction. *J. Phys. Energy* **2025**, *7*, 045030. [CrossRef]
70. Jones, G.; Jakobsen, J.G.; Shim, S.S.; Kleis, J.; Andersson, M.P.; Rossmeisl, J.; Abild-Pedersen, F.; Bligaard, T.; Helveg, S.; Hinnemann, B.; et al. First principles calculations and experimental insight into methane steam reforming over transition metal catalysts. *J. Catal.* **2008**, *259*, 147–160. [CrossRef]
71. Norskov, J.K.; Bligaard, T.; Logadottir, A.; Kitchin, J.; Chen, J.G.; Pandelov, S.; Norskov, J. Trends in the exchange current for hydrogen evolution. *J. Electrochem. Soc.* **2005**, *152*, J23–J26. [CrossRef]
72. Chan, K.; Nørskov, J.K. Electrochemical barriers made simple. *J. Phys. Chem. Lett.* **2015**, *6*, 2663–2668. [CrossRef]
73. Swank, R.K. Surface Properties of II-VI Compounds. *Phys. Rev.* **1967**, *153*, 844. [CrossRef]
74. Gouveia, A.F.; Lemos, S.C.; Leite, E.R.; Longo, E.; Andrés, J. Back to the Basics: Probing the Role of Surfaces in the Experimentally Observed Morphological Evolution of ZnO. *Nanomaterials* **2023**, *13*, 978. [CrossRef]
75. Dengo, N.; Vittadini, A.; Natile, M.M.; Gross, S. In-depth study of ZnS nanoparticle surface properties with a combined experimental and theoretical approach. *J. Phys. Chem. C* **2020**, *124*, 7777–7789. [CrossRef]
76. Jin, Y.; Kim, S.; Yoon, Y.G.; Lee, T.; Chang, J.B.; Lee, K.S.; Ahn, N.; Kim, R.; Park, Y.g.; Lee, J. Defect-Cascades-Induced Photodegradation in InP/ZnSe/ZnS Quantum Dots. *Adv. Sci.* **2025**, *13*, e15691. [CrossRef]
77. Jrad, A.; Naffouti, W.; Nefzi, C.; Ben Nasr, T.; Ammar, S.; Turki-Kamoun, N. Effect of copper concentration on the physical properties of ZnS: Cu alloys prepared by chemical bath deposition. *J. Mater. Sci. Mater. Electron.* **2016**, *27*, 10684–10695. [CrossRef]

78. Morales-Mendoza, J.; Herrera-Pérez, G.; Fuentes-Cobas, L.; Hermida-Montero, L.; Pariona, N.; Paraguay-Delgado, F. Synthesis, structural and optical properties of Cu doped ZnO and CuO–ZnO composite nanoparticles. *Nano-Struct. Nano-Objects* **2023**, *34*, 100967. [CrossRef]
79. VandeVondele, J.; Krack, M.; Mohamed, F.; Parrinello, M.; Chassaing, T.; Hutter, J. Quickstep: Fast and Accurate Density Functional Calculations Using a Mixed Gaussian and Plane Waves Approach. *Comput. Phys. Commun.* **2005**, *167*, 103–128. [CrossRef]
80. VandeVondele, J.; Hutter, J. Gaussian Basis Sets for Accurate Calculations on Molecular Systems in Gas and Condensed Phases. *J. Chem. Phys.* **2007**, *127*, 114105. [CrossRef]
81. Kühne, T.D.; Iannuzzi, M.; Del Ben, M.; Rybkin, V.V.; Seewald, P.; Stein, F.; Laino, T.; Khaliullin, R.Z.; Schütt, O.; Schiffmann, F.; et al. CP2K: An Electronic Structure and Molecular Dynamics Software Package-Quickstep: Efficient and Accurate Electronic Structure Calculations. *J. Chem. Phys.* **2020**, *152*, 194103. [CrossRef]
82. Hartwigsen, C.; Gœdecker, S.; Hutter, J. Relativistic Separable Dual-Space Gaussian Pseudopotentials from H to Rn. *Phys. Rev. B* **1998**, *58*, 3641. [CrossRef]
83. Guidon, M.; Schiffmann, F.; Hutter, J.; VandeVondele, J. Ab Initio Molecular Dynamics Using Hybrid Density Functionals. *J. Chem. Phys.* **2008**, *128*, 214104. [CrossRef] [PubMed]
84. Guidon, M.; Hutter, J.; VandeVondele, J. Robust Periodic Hartree- Fock Exchange for Large-Scale Simulations Using Gaussian Basis Sets. *J. Chem. Theory Comput.* **2009**, *5*, 3010–3021. [CrossRef]
85. Guidon, M.; Hutter, J.; VandeVondele, J. Auxiliary Density Matrix Methods for Hartree-Fock Exchange Calculations. *J. Chem. Theory Comput.* **2010**, *6*, 2348–2364. [CrossRef]
86. Ambrosio, F.; Landi, A.; Loriso, M.; Leo, A.; Peluso, A. External Reorganization Energy upon Charge Transfer Reactions in Mildly Polar Media: The Case of Naphthalene in Tetrahydrofuran. *J. Phys. Chem. Lett.* **2025**, *16*, 6734–6744. [CrossRef]
87. Perdew, J.P.; Ernzerhof, M.; Burke, K. Rationale for Mixing Exact Exchange with Density Functional Approximations. *J. Chem. Phys.* **1996**, *105*, 9982–9985. [CrossRef]
88. Adamo, C.; Barone, V. Toward reliable density functional methods without adjustable parameters: The PBE0 model. *J. Chem. Phys.* **1999**, *110*, 6158–6170. [CrossRef]
89. Miceli, G.; Chen, W.; Reshetnyak, I.; Pasquarello, A. Nonempirical Hybrid Functionals for Band Gaps and Polaronic Distortions in Solids. *Phys. Rev. B* **2018**, *97*, 121112. [CrossRef]
90. Bischoff, T.; Reshetnyak, I.; Pasquarello, A. Adjustable Potential Probes for Band-Gap Predictions of Extended Systems through Nonempirical Hybrid Functionals. *Phys. Rev. B* **2019**, *99*, 201114. [CrossRef]
91. Perdew, J.P.; Zunger, A. Self-Interaction Correction to Density-Functional Approximations for Many-Electron Systems. *Phys. Rev. B* **1981**, *23*, 5048–5079. [CrossRef]
92. Zhang, Y.; Yang, W. A Challenge for Density Functionals: Self-interaction Error Increases for Systems with a Noninteger Number of Electrons. *J. Chem. Phys.* **1998**, *109*, 2604–2608. [CrossRef]
93. Ambrosio, F.; Wiktor, J. Charge Localization in Optoelectronic and Photocatalytic Applications: Computational perspective. *Appl. Phys. Lett.* **2025**, *126*, 130501. [CrossRef]
94. Janak, J.F. Proof that $\frac{\partial E}{\partial n_i} = \epsilon$ in Density-Functional Theory. *Phys. Rev. B* **1978**, *18*, 7165–7168. [CrossRef]
95. Yang, W.; Zhang, Y.; Ayers, P.W. Degenerate Ground States and a Fractional Number of Electrons in Density and Reduced Density Matrix Functional Theory. *Phys. Rev. Lett.* **2000**, *84*, 5172–5175. [CrossRef] [PubMed]
96. Perdew, J.P.; Parr, R.G.; Levy, M.; Balduz, J.L. Density-Functional Theory for Fractional Particle Number: Derivative Discontinuities of the Energy. *Phys. Rev. Lett.* **1982**, *49*, 1691–1694. [CrossRef]
97. Yang, J.; Falletta, S.; Pasquarello, A. Range-separated Hybrid Functionals for Accurate Prediction of Band Gaps of Extended Systems. *npj Comput. Mater.* **2023**, *9*, 108. [CrossRef]
98. Ambrosio, F.; Miceli, G.; Pasquarello, A. Redox Levels in Aqueous Solution: Effect of van der Waals Interactions and Hybrid Functionals. *J. Chem. Phys.* **2015**, *143*, 244508. [CrossRef] [PubMed]
99. Alkauskas, A.; Broqvist, P.; Pasquarello, A. Defect Energy Levels in Density Functional Calculations: Alignment and Band Gap Problem. *Phys. Rev. Lett.* **2008**, *101*, 046405. [CrossRef]
100. Alkauskas, A.; Broqvist, P.; Pasquarello, A. Defect Levels through Hybrid Density Functionals: Insights and Applications. *Phys. Status Solidi B* **2011**, *248*, 775–789. [CrossRef]
101. Halgren, T.A.; Lipscomb, W.N. The synchronous-transit method for determining reaction pathways and locating molecular transition states. *Chem. Phys. Lett.* **1977**, *49*, 225–232. [CrossRef]
102. Hou, Q.; Buckeridge, J.; Walsh, A.; Xie, Z.; Lu, Y.; Keal, T.W.; Guan, J.; Woodley, S.M.; Catlow, C.R.A.; Sokol, A.A. The Interplay of Interstitial and Substitutional Copper in Zinc Oxide. *Front. Chem.* **2021**, *9*, 780935. [CrossRef] [PubMed]
103. Mang, A.; Reimann, K.; Rübenacke, S. Band gaps, crystal-field splitting, spin-orbit coupling, and exciton binding energies in ZnO under hydrostatic pressure. *Solid State Commun.* **1995**, *94*, 251–254. [CrossRef]

104. Mang, A.; Reimann, K.; Steube, M. Two-photon spectroscopy study of ZnS and CdS under hydrostatic pressure. *Phys. Rev. B* **1996**, *53*, 16283. [CrossRef] [PubMed]
105. Agarwal, D.; Singh, U.; Gupta, S.; Singhal, R.; Kulriya, P.; Singh, F.; Tripathi, A.; Singh, J.; Joshi, U.; Avasthi, D. Enhanced room temperature ferromagnetism and green photoluminescence in Cu doped ZnO thin film synthesised by neutral beam sputtering. *Sci. Rep.* **2019**, *9*, 6675. [CrossRef]
106. Kawai, H.; Kuboniwa, S.; Hoshina, T. Concentration dependence of green-Cu luminescence in ZnS: Cu, Al. *Jpn. J. Appl. Phys.* **1974**, *13*, 1593. [CrossRef]
107. Godby, R.W.; Needs, R. Metal-insulator transition in Kohn-Sham theory and quasiparticle theory. *Phys. Rev. Lett.* **1989**, *62*, 1169. [CrossRef]
108. Ambrosio, F.; Guo, Z.; Pasquarello, A. Absolute Energy Levels of Liquid Water. *J. Phys. Chem. Lett.* **2018**, *9*, 3212–3216. [CrossRef] [PubMed]
109. Zhang, L.; Jaroniec, M. Fundamentals of adsorption for photocatalysis. *Interface Sci. Technol.* **2020**, *31*, 39–62.
110. Ricciarelli, D.; Mosconi, E.; Wiktor, J.; Malavasi, L.; Ambrosio, F.; De Angelis, F. Electron Bipolarons at the DMASnBr$_3$–Water Interface: Effect on the Photocatalytic Hydrogen Production. *Int. J. Hydrogen Energy* **2024**, *58*, 863–871. [CrossRef]
111. Nørskov, J.K.; Bligaard, T.; Rossmeisl, J.; Christensen, C.H. Towards the computational design of solid catalysts. *Nat. Chem.* **2009**, *1*, 37–46. [CrossRef] [PubMed]
112. Conway, B.; Tilak, B. Interfacial processes involving electrocatalytic evolution and oxidation of H_2, and the role of chemisorbed H. *Electrochim. Acta* **2002**, *47*, 3571–3594. [CrossRef]
113. Guo, Z.; Ambrosio, F.; Chen, W.; Gono, P.; Pasquarello, A. Alignment of Redox Levels at Semiconductor–Water Interfaces. *Chem. Mater.* **2018**, *30*, 94–111. [CrossRef]
114. Guo, Z.; Ambrosio, F.; Pasquarello, A. Evaluation of Photocatalysts for Water Splitting through Combined Analysis of Surface Coverage and Energy-Level Alignment. *ACS Catal.* **2020**, *10*, 13186–13195. [CrossRef]
115. Cramer, C. J. *Essentials of Computational Chemistry: Theories and Models*; John Wiley & Sons: Hoboken, NJ, USA, 2013.
116. Gono, P.; Wiktor, J.; Ambrosio, F.; Pasquarello, A. Surface Polarons Reducing Overpotentials in the Oxygen Evolution Reaction. *ACS Catal.* **2018**, *8*, 5847–5851. [CrossRef]
117. Wyckoff, R. Interscience Publishers, New York, New York Rocksalt Structure. *Cryst. Struct.* **1963**, *1*, 85–237.
118. Yeh, C.-Y.; Lu, Z. W.; Froyen, S.; Zunger, A. Zinc-blende–wurtzite polytypism in semiconductors. *Phys. Rev. B* **1992**, *46*, 10086–10097. [CrossRef] [PubMed]
119. Janosi, A. La structure du sulfure cuivreux quadratique. *Acta Crystallogr.* **1964**, *17*, 311–312. [CrossRef]
120. Evans, H.T.; Konnert, J.A. Crystal structure refinement of covellite. *Am. Mineral.* **1976**, *61*, 996–1000.
121. Kjekshus, A.; Rakke, T. Preparations and properties of magnesium, copper, zinc and cadmium dichalcogenides. *Acta Chem. Scand.* **1979**, *33*, 617. [CrossRef]
122. Rahlfs, P. Über die kubischen Hochtemperaturmodifikationen der Sulfide, Selenide und Telluride des Silbers und des einwertigen Kupfers. *Z. Phys. Chem.* **1936**, *31*, 157–194. [CrossRef]
123. Berry, L.G. The crystal structure of covellite, CuSe and klockmannite, CuSe. *Am. Mineral.* **1954**, *39*, 504–509.
124. Heyding, R.D. The copper/selenium system. *Can. J. Chem.* **1966**, *44*, 1233–1236. [CrossRef]
125. Pawley, G.S.; Rinaldi, R.P. Constrained refinement of orthorhombic sulphur. *Acta Crystallogr. Sect. B* **1972**, *28*, 3605–3609. [CrossRef]
126. McCann, D.R.; Cartz, L. Bond distances and chain angle of hexagonal selenium at high pressure. *J. Appl. Phys.* **1972**, *43*, 4473–4477. [CrossRef]
127. Kaur, K.; Singh, C.V. Amorphous TiO_2 as a photocatalyst for hydrogen production: A DFT study of structural and electronic properties. *Energy Procedia* **2012**, *29*, 291–299. [CrossRef]

Disclaimer/Publisher's Note: The statements, opinions and data contained in all publications are solely those of the individual author(s) and contributor(s) and not of MDPI and/or the editor(s). MDPI and/or the editor(s) disclaim responsibility for any injury to people or property resulting from any ideas, methods, instructions or products referred to in the content.